Manuscript title: An unconstrained stress updating algorithm with the line search method for elastoplastic soil models

Authors: Xin Zhou[1], Dechun Lu[1], Cancan Su[1], Zhiwei Gao[2], Xiuli Du[1]

Affiliations: [1]Institute of Geotechnical and Underground Engineering, Beijing University of Technology, Beijing, Beijing 100124, China; [2]James Watt School of Engineering, University of Glasgow, Glasgow, G12 8QQ, UK.

Corresponding author: Dechun Lu

E-mail: dechun@bjut.edu.cn

Abstract

This paper is devoted to developing an efficient and robust stress updating algorithm in a relatively simple computational framework to address the two difficulties of implementing elastoplastic soil models, namely the nonsmoothness and the nonlinearity. In the proposed algorithm, the nonsmoothness caused by the loading/unloading inequality constraints is eliminated by replacing the *Karush-Kuhn-Tucker* conditions with the smoothing function. The stress updating can be achieved by solving a set of smooth nonlinear algebraic equations in this algorithm. The nonlinear equations are solved using the line search method, which allows a larger convergence radius of the solution in contrast to the standard Newton method. Meanwhile, the smoothing consistent tangent operator corresponding to the unconstrained stress updating strategy ensures the quadratic convergence speed of the global solution. The modified Cam-clay model is used as an example to demonstrate the implementation of this algorithm. The correctness, computational efficiency, and robustness of the algorithm are validated and assessed by comparing it with the analytical solutions in case of cylindrical cavity expansion and the ABAQUS/Standard default integration method. In simulations with large load increment sizes, the CPU time consumed by the new algorithm can be less than half of the ABAQUS default algorithm.

Keywords: Constitutive model integration; Line search method; Smoothing function; Modified Cam-clay model; soil; Consistent tangent operator

Notation

$\boldsymbol{\sigma}$, $\mathbf{s}$	stress tensor, deviatoric stress tensor
p, q	mean effective stress, generalized shear stress
p_c	pre-consolidation pressure
$\boldsymbol{\varepsilon}$, $\boldsymbol{\varepsilon}^e$, $\boldsymbol{\varepsilon}^p$	total, elastic, and plastic strain tensors
ε_v, ε_v^e, ε_v^p	total, elastic, and plastic volume strains
$\boldsymbol{\gamma}$, $\boldsymbol{\gamma}^p$	total and plastic deviatoric strain increment tensors
K, G	bulk modulus, shear modulus
ν	Poisson's ratio
$\mathbf{D}$	elastic stiffness tensor
λ, κ	compression index, the swell index in the isotropic compression test
e_0, e_1	initial void ratio, void ratio at $p = 1$ kPa
M	slope of the critical state line
γ_w	unit weight
$\mathbf{1}$, $\mathbf{I}$	second-order unit tensor, fourth-order unit tensor
$\mathbf{I}^{vol}$, $\mathbf{I}^{sym}$	volumetric and symmetric fourth-order unit tensors
$\mathbf{P}$	fourth-order projection tensor
f	yield function
H	plastic internal variable
h	plastic modulus
$\mathbf{r}$	plastic flow direction
ϕ	plastic multiplier
c_d	dimensional parameter
β	smoothing parameter
ρ, ς	algorithm parameters in the line search method
α	step size of the search direction
$\mathbf{d}$	search direction vector
ψ, $\hat{\psi}$	merit function, the approximation of merit function
K_0	coefficient of earth pressure at rest
OCR	overconsolidation ratio
v	specific volume

1. Introduction

The elastoplastic soil models have been an essential cornerstone in the numerical analysis of geotechnical problems (Zhang *et al.* 2020). Numerous elastoplastic soil models have been proposed to describe the complex mechanical behaviour of various soils under different load conditions (Dafalias 1980; Hashiguchi 1989; Gao *et al.* 2014; Yao *et al.* 2014; Liang *et al.* 2019; Xiao & Desai 2019; Sun *et al.* 2020; Gao & Diambra 2021). For instance, the Cam-clay model (Roscoe & Schofield 1963; Schofield & Wroth 1968) and the modified Cam-clay (MCC) model (Roscoe & Burland 1968) which are developed within the critical state soil mechanics framework have been widely used in analysing various geotechnical problems. The elastoplastic soil models are generally complex, which makes the numerical implementation in a finite element code challenging. Therefore, a lot of attempts have been made to address the stress updating of elastoplastic soil models (Borja & Lee 1990; Borja 1991; Sheng *et al.* 2000; Sloan *et al.* 2001; Zhao *et al.* 2005; Krabbenhoft *et al.* 2007; Krabbenhoft & Lyamin 2012; Geng *et al.* 2021).

In the numerical implementation, an elastoplastic model defined in ordinary differential equations is discretized as a set of algebraic equations constrained by the *Karush-Kuhn-Tucker* (*KKT*) conditions containing the loading/unloading inequality. There are usually two difficulties in solving the constrained nonlinear equations, i.e., the nonsmoothness induced by the *KKT* conditions and the nonlinearity of the constitutive equations. In most stress integration methods, the operator split method is the most commonly used treatment for the loading/unloading inequality constraints (Simo & Hughes 2006). In this method, the trial stress obtained by the elastic predictor is used to estimate the stress behaviour (i.e., elasticity or plasticity) under the current increment step. The

integration formulas that match the stress behaviour are then chosen to calculate the new state variables satisfying the *KKT* conditions. The operator split method has been incorporated into several typical stress updating algorithms, e.g., the full-implicit return-mapping algorithm (Ortiz & Simo 1986), the cutting-plane algorithm (Simo & Ortiz 1985; Starman *et al.* 2014), and the semi-implicit algorithm (Moran *et al.* 1990). However, the operator splitting inevitably leads to increased algorithm complexity since the loading/unloading estimations based on the elastic predictor have to be executed in the calculation of each step. Particular attention must be paid to the stress behaviour transition from elasticity to plasticity in a load increment when the explicit integration scheme is employed (Sloan *et al.* 2001).

There are also some other methods to address the constrained optimization problems in numerical optimization (Nocedal & Wright 2006). One is to directly solve the constrained optimization problem, e.g., the projection gradient method and the Zoutendijk feasible direction method (Nocedal & Wright 2006). The search direction of each iteration is both the descending direction of the merit function and the feasible direction of the constraint functions. For example, Zheng *et al.* (2020) have used the projection-contraction method for the implementation of the Mohr-Coulomb plasticity model. Few model implementations have been, however, developed along this line, probably due to its tedious constraint correction process (Arora 2016). Another more popular idea is to use the penalty function or the smoothing function to convert inequality constraints into equality constraints, which are then added to the merit function. Then all that remains is to solve an unconstrained optimization problem. The penalty function-based optimization methods mainly include the Lagrangian method (Contrafatto & Cuomo 2005), the multiplier method (Contrafatto &

Cuomo 2005), and the interior method (Krabbenhoft *et al.* 2007). The Lagrangian method and multiplier method applications to the mixed Hellinger-Reissner functional governing the elastoplasticity problem are explored by Contrafatto & Cuomo (2005). The important contributions of this study are that the *KKT* conditions are equivalently replaced by an equality constraint with the Max function and the multiplier method affects the entire equilibrium iterations. However, it is worth noting that the nonsmoothness of the elastoplastic problem is not eliminated in essence but shifted to the Max function. Krabbenhoft *et al*. (2007) presented a detailed application of the primal-dual interior-point method in the perfect plasticity, hardening multisurface plasticity, and softening plasticity, in which the elastoplastic problem's finite element scheme is recast into a second-order cone scheme to solve. Then, a similar computational framework was extended further to the implementation of the MCC model by Krabbenhoft & Lyamin (2012).

A more cost-effective and promising method to eliminate the nonsmoothness of elastoplastic problems is to directly use a single smoothing function to replace two inequality constraints and one equality constraint in *KKT* conditions (Areias & Rabczuk 2010). The updating of state variables in both the elastic and elastoplastic loading cases can be accomplished using integral equations with the unified form. Estimations for loading/unloading are also unnecessary. This method has great potential in streamlining the stress updating procedure (Scalet & Auricchio 2018). But its applications to elastoplasticity models are rare. There are just a few reports about the application of the smoothing function in crystal plasticity (Schmidt-Baldassari 2003; Akpama *et al.* 2016) and finite strain plasticity (Areias *et al.* 2012; Areias *et al.* 2015). It is worthwhile to investigate recasting the stress updating strategy of elastoplastic soil models with the smoothing function.

After addressing the nonsmoothness generated by the *KKT* conditions, the solution of nonlinear stress integration equations (or the solution of unconstrained optimization problem) is another challenge we have to face. In the implicit stress updating algorithms (Simo & Ortiz 1985; Ortiz & Simo 1986; Moran *et al.* 1990), the Newton method has been widely used due to its asymptotic quadratic convergence speed (Potts *et al.* 2021). The researchers have noted, however, that the Newton method's convergence is significantly dependent on the proximity between the initial value and the final solution (Brannon & Leelavanichkul 2010; Scalet & Auricchio 2018). The optimal convergence property may be lost when the iteration point exceeds the convergence radius of the Newton method or the Taylor series used in the Newton method is difficult to approximate the original problem well in the vicinity of the solution due to the presence of strong nonlinearity (Contrafatto & Cuomo 2005). Various efforts have been made to close the gap, including the proposal of some corrective measures, e.g., optimizing the initial iteration point (Hernández *et al.* 2011), sub-stepping schemes (Pérez-Foguet *et al.* 2001; Wang *et al.* 2006), and multi-stage iteration (Homel *et al.* 2015; Homel & Brannon 2015), as well as the use of optimization methods with the strong convergence, e.g., the line search method (LSM) (Dutko *et al.* 1993; Pérez-Foguet & Armero 2002; Seifert & Schmidt 2008; Scherzinger 2017), the trust region method (Shterenlikht & Alexander 2012; Lester & Scherzinger 2017), and the homotopy method (Geng *et al.* 2021). The LSM is more widely used due to its appealing simplicity and practicability. Unlike the trust region method, which must take into account the poor scaling problem (Lester & Scherzinger 2017), or the homotopy method, which must solve a series of homotopy equations of the original problem to obtain a better iteration point (Geng *et al.* 2021), the LSM only needs to determine an optimal step

size additionally under a given search direction to obtain a larger convergence radius. It also has at least quadratic convergence speed if the newton direction is chosen as the search direction. The optimal step size can be obtained through a simple iteration formula that does not require the calculation of the Jacobian matrix (Scherzinger 2017). The performance of the LSM has been thoroughly tested in the numerical implementation of some isotropic and anisotropic metal models (Scherzinger 2017; Choi & Yoon 2019; Yoon *et al.* 2020). Though efficient and robust, this method has not been used in implementing elastoplastic soil models, which are typically more difficult than the mental models because soils have stronger nonlinear characteristics, e.g., strain hardening/softening, volume expansion/contraction, pressure-dependency during shear, etc.

The motivation of this work is to present a low-cost, efficient and robust stress updating algorithm for elastoplastic soil models based on the appropriate optimization methods. The elastoplastic model's nonsmoothness and nonlinearity will be addressed by using the smoothing function and the LSM, respectively. In the remainder of the paper, an unconstrained stress updating strategy without the need for the loading/unloading estimations is developed by replacing the *KKT* conditions with the smoothing function. Under this computational framework, the MCC model is used as an application object of the proposed algorithm. The backward Euler integration scheme is used to obtain the stress integration equations of the model. Furthermore, the nonlinear stress integration equations are solved by the LSM. The smoothing consistent tangent operator (CTO) corresponding to the unconstrained stress updating strategy is derived. Finally, compared with the ABAQUS/Standard default integration method (DIM), the correctness, the robustness, and the

computational efficiency of the proposed algorithm are verified and assessed based on four typical boundary value problems.

2. Unconstrained stress updating strategy

For a classical rate-independent elastoplastic constitutive model, the mathematical equations describing the stress-strain relationship are generally defined by a set of ordinary differential equations with constraints as follows:

$$\begin{aligned} &\dot{\boldsymbol{\sigma}} = \mathbf{D} : \dot{\boldsymbol{\varepsilon}}^{\mathrm{e}} = \mathbf{D} : \left(\dot{\boldsymbol{\varepsilon}} - \dot{\boldsymbol{\varepsilon}}^{\mathrm{p}} \right) \\ &\dot{\boldsymbol{\varepsilon}}^{\mathrm{p}} = \dot{\phi} \mathbf{r} \\ &\dot{H} = \dot{\phi} h \\ &\dot{\phi} \geq 0,\ f \leq 0,\ \dot{\phi} f = 0 \end{aligned} \tag{1}$$

where the four parts of Eq. (1) are known as Hooke's Law, flow rule, hardening law, and the *KKT* conditions, respectively. $\mathbf{D}$ is the elastic stiffness and $\mathbf{D} = \mathbf{I}^{\mathrm{vol}} \left(3K - 2G \right) + 2\mathbf{I}^{\mathrm{sym}} G$, where $\mathbf{I}^{\mathrm{vol}}$ and $\mathbf{I}^{\mathrm{sym}}$ are the volumetric and symmetric fourth-order unit tensors, respectively. K and G denote the elastic bulk modulus and shear modulus, respectively. $\dot{\boldsymbol{\sigma}}$, $\dot{\boldsymbol{\varepsilon}}$, $\dot{\boldsymbol{\varepsilon}}^{\mathrm{e}}$, $\dot{\boldsymbol{\varepsilon}}^{\mathrm{p}}$, and $\dot{H}$ are the rates of the stress tensor, total strain tensor, elastic strain tensor, plastic strain tensor, and the plastic internal variable, respectively. $\mathbf{r}$ and h denote the direction of the plastic flow rule and hardening, respectively. f and $\dot{\phi}$ are the yield function and plastic multiplier, respectively. Note that the *KKT* constrains the allowable state variables, namely, $\dot{\phi} \geq 0$ and $f\left(\boldsymbol{\sigma}, H\right) = 0$ for loading, and $\dot{\phi} = 0$ and $f \leq 0$ for unloading. The constitutive equations in Eq. (1) are defined in rate form. In the numerical implementation, it needs to be discretized into algebraic equations in time by a specific integral scheme. For instance, the equations to be solved for the backward Euler integration scheme are:

$$
\begin{aligned}
&\boldsymbol{\sigma}_{n+1} = \boldsymbol{\sigma}_n + \mathbf{D} : \left(\Delta\boldsymbol{\varepsilon}_{n+1} - \Delta\boldsymbol{\varepsilon}^{\mathrm{p}}_{n+1} \right) \\
&\Delta\boldsymbol{\varepsilon}^{\mathrm{p}}_{n+1} = \Delta\phi_{n+1}\mathbf{r}_{n+1} \\
&\Delta H_{n+1} = \Delta\phi_{n+1} h_{n+1} \\
&\Delta\phi_{n+1} \geq 0,\ f_{n+1} \leq 0,\ \Delta\phi_{n+1} f_{n+1} = 0
\end{aligned}
\tag{2}
$$

The aim of the stress updating algorithm is to solve Eq. (2) based on a given set of state variables $\left(\boldsymbol{\sigma}_n, H_n\right)$ at step n and the strain increment $\Delta\boldsymbol{\varepsilon}_{n+1}$ to obtain the state variables $\left(\boldsymbol{\sigma}_{n+1}, H_{n+1}\right)$ at step $n+1$. Note that the difficulty of solving Eq. (2) lies mainly in nonsmoothness caused by inequality constraints and the nonlinearity of f, $\mathbf{r}$, h, and $\mathbf{D}$.

For the inequality constraints in Eq. (2), the classical operator splitting technique appears to provide good treatment. In this stress updating strategy, the inequality constraints are first activated by the elastic predictor, where the trial stress is computed by $\boldsymbol{\sigma}^{trial}_{n+1} = \boldsymbol{\sigma}_n + \mathbf{D} : \Delta\boldsymbol{\varepsilon}_{n+1}$. Then, the trial stress inside the yield surface (i.e., $f\left(\boldsymbol{\sigma}^{trial}_{n+1}, H_n\right) \leq 0$) is accepted as the true stress at step $n+1$, whereas the trial stress on the outside of the yield surface (i.e., $f\left(\boldsymbol{\sigma}^{trial}_{n+1}, H_n\right) > 0$) is pulled back to the yield surface by the plastic corrector if the return-mapping algorithm is used, as shown in Fig. 1.

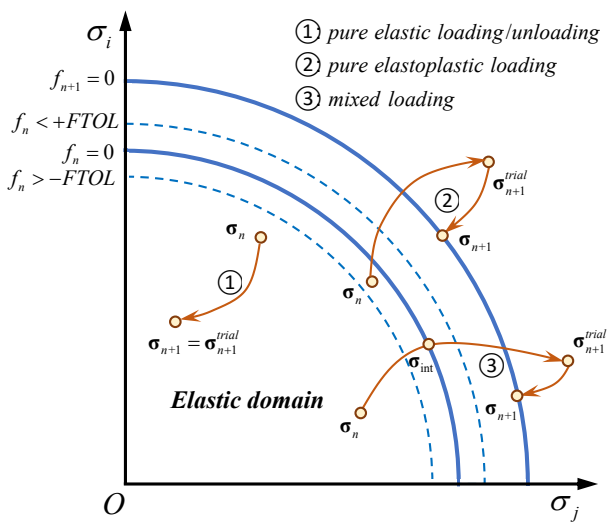

Fig. 1 Operator splitting stress updating strategy.

The nonsmoothness of the elastoplastic problem is inherited from the *KKT* conditions defined by Eq. (2). In numerical optimization, the nonsmooth *KKT* conditions can be replaced equivalently by the smoothing function, and then Eq. (2) is transformed into the smooth version shown below:

$$\begin{aligned}
&\boldsymbol{\sigma}_{n+1} = \boldsymbol{\sigma}_n + \mathbf{D} : \left(\Delta\boldsymbol{\varepsilon}_{n+1} - \Delta\boldsymbol{\varepsilon}^{\mathrm{p}}_{n+1} \right) \\
&\Delta\boldsymbol{\varepsilon}^{\mathrm{p}}_{n+1} = \Delta\phi_{n+1}\mathbf{r}_{n+1} \\
&\Delta H_{n+1} = \Delta\phi_{n+1} h_{n+1} \\
&\sqrt{\left(c_{\mathrm{d}}\Delta\phi_{n+1}\right)^2 + f_{n+1}^2 + 2\beta} - c_{\mathrm{d}}\Delta\phi_{n+1} + f_{n+1} = 0
\end{aligned} \tag{3}$$

where the *Fischer-Burmeister* (*FB*) function, i.e., Eq. $(3)_4$ is employed (Fischer 1992; Kanzow 1996). c_{d} is a dimensional parameter. Fig. 2 shows the effect of β on the *FB* smoothing curve. The smoothing function converges to the *KKT* conditions when β trends to 0. Note that the smooth function has a higher curvature near the origin. However, the influence of this high curvature phenomenon on the calculation can be eliminated by selecting the elastic trial point as the initial point of iteration. This means that if the current step is elastic, the trial point is accepted and there is no need for the next iteration. If the current step is plastic, both the initial iteration point, i.e., $\left(f_{n+1}^0 \left(\boldsymbol{\sigma}_{n+1}^{trial}, H_n \right) > 0,\ \Delta\phi_{n+1}^0 = 0 \right)$ and the convergent iteration point, i.e., $\left(f_{n+1} \left(\boldsymbol{\sigma}_{n+1}, H_{n+1} \right) = 0,\ \Delta\phi_{n+1} > 0 \right)$ are far away from the origin of the smooth curve. The search process of solution does involve areas of high curvature.

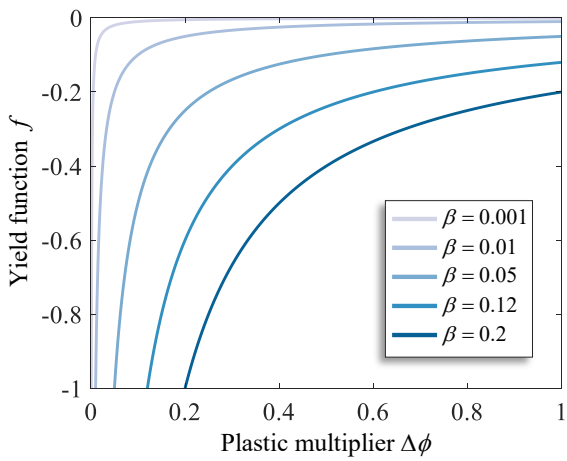

Fig. 2 Smoothing curves with the different values of β.

By using the *FB* smooth function instead of *KKT* conditions, Eq. (3) can give rise to an unconstrained stress updating strategy without the need for loading/unloading estimations, as shown in Fig. 3. The stress states on both the elastic domain and yield surfaces, as illustrated in Fig. 2, are projected onto a smooth curve. As a result, the stress-strain behaviour under the pure elastic loading/unloading condition, elastoplastic loading, and mixed loading can be described uniformly by a set of smooth equations. Under this computational paradigm, one of the difficulties in solving the elastoplastic problems, i.e., the nonsmoothness, can be bypassed. The only change required is to use the smoothing function instead of *KKT* conditions. More focus should be placed on the treatment of nonlinearity in Eq. (3).

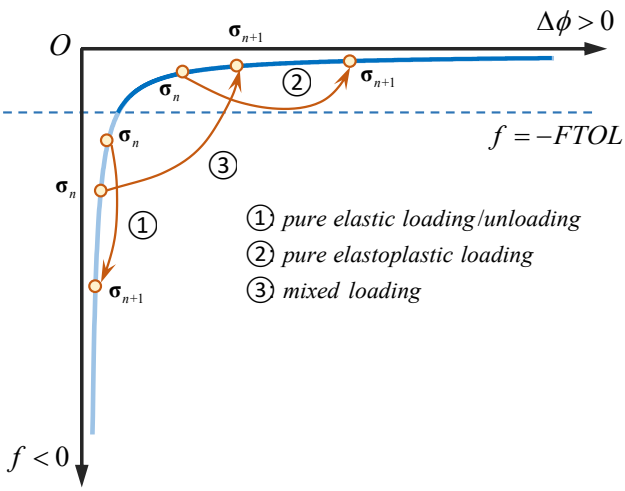

Fig. 3 Unconstrained stress updating strategy.

3. Integral formulas of MCC model

Eq. (3) only presents the general integral formulas of the unconstrained stress updating strategy. Specific expressions for the yield function, the flow direction, the hardening law, and the elastic law do need to be specified when applied to the elastoplastic soil models. In this section, the MCC model is considered as an example due to its broad application in geotechnical engineering.

In the MCC model, the yield function in elliptical form is employed to determine the elastic domain of material:

$$f_{n+1} = \frac{q_{n+1}^2}{M^2} + p_{n+1}\left(p_{n+1} - p_{\mathrm{c},\,n+1}\right) \tag{4}$$

where M denotes the slope of the critical state line in the p-q space. p_{n+1} and q_{n+1} are the mean effective stress and generalized shear stress. The hardening law of the MCC model is defined by the evolution equation for the pre-consolidation pressure $p_{\mathrm{c},\,n+1}$, which is the function of plastic volume strain increment $\Delta\varepsilon_{\mathrm{v},\,n+1}^{\mathrm{p}}$ as follows:

$$p_{\mathrm{c},\,n+1} = p_{\mathrm{c},\,n}\exp\left(c_{\mathrm{p}}\Delta\varepsilon_{\mathrm{v},\,n+1}^{\mathrm{p}}\right) \tag{5}$$

where $c_{\mathrm{p}} = \left(1+e_0\right)/\left(\lambda-\kappa\right)$. λ, κ, and e_0 denote the compression index, swell index, and the initial void ratio, respectively.

The plastic flow direction of the MCC model is expressed as

$$\Delta\boldsymbol{\varepsilon}_{n+1}^{\mathrm{p}} = \Delta\phi_{n+1}\frac{\partial f_{n+1}}{\partial\boldsymbol{\sigma}_{n+1}} = \frac{3\mathbf{s}_{n+1}}{M^2}\Delta\phi_{n+1} + \frac{\left(2p_{n+1} - p_{\mathrm{c},\,n+1}\right)\mathbf{1}}{3}\Delta\phi_{n+1} \tag{6}$$

where $\mathbf{s}_{n+1} = \boldsymbol{\sigma}_{n+1} - p_{n+1}\mathbf{1}$ denotes the deviatoric stress tensor and $\mathbf{1}$ is the second-order unit tensor. Based on Eq. (6), the expressions of plastic volume strain increment $\Delta\varepsilon_{\mathrm{v},\,n+1}^{\mathrm{p}}$ and deviatoric strain increment tensor $\Delta\boldsymbol{\gamma}_{n+1}^{\mathrm{p}}$ can be obtained as follows:

$$\Delta\varepsilon_{\mathrm{v},\,n+1}^{\mathrm{p}} = \Delta\boldsymbol{\varepsilon}_{n+1}^{\mathrm{p}} : \mathbf{1} = \Delta\phi_{n+1}\left(2p_{n+1} - p_{\mathrm{c},\,n+1}\right) \tag{7}$$

$$\Delta\boldsymbol{\gamma}_{n+1}^{\mathrm{p}} = \frac{3\mathbf{s}_{n+1}}{M^2}\Delta\phi_{n+1} \tag{8}$$

Substituting Eq. (7) into Eq. (5), the updating formula of $p_{\mathrm{c},\,n+1}$ can be rewritten as follows:

$$p_{\mathrm{c},\,n+1} = p_{\mathrm{c},\,n}\exp\left[c_{\mathrm{p}}\Delta\phi_{n+1}\left(2p_{n+1} - p_{\mathrm{c},\,n+1}\right)\right] \tag{9}$$

For the MCC model, the updating formula of the stress tensor in Eq. (3) can be replaced by the mean effective stress p_{n+1} and the generalized shear stress q_{n+1} to reduce the number of integration equations:

$$p_{n+1} = \frac{1}{3}\boldsymbol{\sigma}_{n+1} : \mathbf{1} = p_n + \bar{K}\left(\Delta\varepsilon_{\mathrm{v},\, n+1} - \Delta\varepsilon^{\mathrm{p}}_{\mathrm{v},\, n+1}\right) \tag{10}$$

$$q_{n+1} = \sqrt{\frac{3}{2}}\left\|\mathbf{s}_{n+1}\right\| \tag{11}$$

where $\Delta\varepsilon_{\mathrm{v},\, n+1}$ is the total volume strain increment. $\bar{K}$ denotes the secant bulk modulus (Borja 1991) and is defined by:

$$\bar{K} = \frac{p_n}{\Delta\varepsilon_{\mathrm{v},\, n+1} - \Delta\varepsilon^{\mathrm{p}}_{\mathrm{v},\, n+1}}\left\{\exp\left[c_\kappa\left(\Delta\varepsilon_{\mathrm{v},\, n+1} - \Delta\varepsilon^{\mathrm{p}}_{\mathrm{v},\, n+1}\right)\right] - 1\right\} \tag{12}$$

where $c_\kappa = \left(1+e_0\right)/\kappa$. The updating formula of $\mathbf{s}_{n+1}$ is determined by:

$$\mathbf{s}_{n+1} = \mathbf{s}_n + 2\bar{G}\left(\Delta\boldsymbol{\gamma}_{n+1} - \Delta\boldsymbol{\gamma}^{\mathrm{p}}_{n+1}\right) \tag{13}$$

where $\bar{G} = \bar{K}r$ is the secant shear modulus. $r = 3\left(1-2\nu\right)/2\left(1+\nu\right)$ where ν is the Poisson's ratio. $\Delta\boldsymbol{\gamma}_{n+1}$ is the total deviatoric strain increment tensor.

Substituting Eqs. (7) and (12) into Eq. (10), one can obtain the updating formula of p_{n+1}:

$$p_{n+1} = p_n \exp\left\{c_\kappa\left[\Delta\varepsilon_{\mathrm{v},\, n+1} - \Delta\phi_{n+1}\left(2p_{n+1} - p_{\mathrm{c},\, n+1}\right)\right]\right\} \tag{14}$$

Substituting Eq. (8) into (13), the updating formula of $\mathbf{s}_{n+1}$ can be rewritten as follows:

$$\mathbf{s}_{n+1} = \frac{\mathbf{s}_n + 2\bar{G}\Delta\boldsymbol{\gamma}_{n+1}}{1 + 6\bar{G}\Delta\phi_{n+1}/M^2} \tag{15}$$

Substituting Eq. (15) into (11), one can obtain the updating formula of q_{n+1} as follows:

$$q_{n+1} = \sqrt{\frac{3}{2}}\frac{\left\|\mathbf{s}_n + 2\bar{G}\Delta\boldsymbol{\gamma}_{n+1}\right\|}{1 + 6\bar{G}\Delta\phi_{n+1}/M^2} \tag{16}$$

After p_{n+1} and q_{n+1} are updated, the stress tensor can be updated by:

$$\boldsymbol{\sigma}_{n+1} = p_{n+1}\mathbf{1} + \mathbf{s}_{n+1} \tag{17}$$

Finally, using the *FB* smoothing function instead of *KKT* conditions and considering Eqs. (9), (14), and (16), a set of closed nonlinear equations $\left\{\mathbf{f}\left(\mathbf{x}\right)\right\}_{n+1}$ including only four independent variables $\left\{\mathbf{x}_{n+1}\right\}=\left\{p_{n+1} \quad q_{n+1} \quad p_{\mathrm{c},\,n+1} \quad \Delta\phi_{n+1}\right\}^{T}$ can be obtained as follows:

$$\begin{Bmatrix} f_1 \\ f_2 \\ f_3 \\ f_4 \end{Bmatrix}=\begin{Bmatrix} p_{n+1}-p_n \exp\left[c_\kappa \Delta\varepsilon_{\mathrm{v},\,n+1}-c_\kappa \Delta\phi_{n+1}\left(2p_{n+1}-p_{\mathrm{c},\,n+1}\right)\right] \\ q_{n+1}-\sqrt{\dfrac{3}{2}}\dfrac{\left\|\mathbf{s}_n+2\bar{G}\Delta\boldsymbol{\gamma}_{n+1}\right\|}{1+6\bar{G}\Delta\phi_{n+1}/M^2} \\ p_{\mathrm{c},\,n+1}-p_{\mathrm{c},\,n}\exp\left[c_{\mathrm{p}}\Delta\phi_{n+1}\left(2p_{n+1}-p_{\mathrm{c},\,n+1}\right)\right] \\ \sqrt{\left(c_{\mathrm{d}}\Delta\phi_{n+1}\right)^2+f_{n+1}^2+2\beta}-c_{\mathrm{d}}\Delta\phi_{n+1}+f_{n+1} \end{Bmatrix}=\begin{Bmatrix} 0 \\ 0 \\ 0 \\ 0 \end{Bmatrix} \tag{18}$$

where c_{d} is recommended equal to $\left\|\boldsymbol{\sigma}_n+\bar{\mathbf{D}}\left(\bar{K},\bar{G}\right):\Delta\boldsymbol{\varepsilon}_{n+1}\right\|^3$ to balance the magnitude and dimension difference between $\Delta\phi_{n+1}$ and f_{n+1}. In this paper, the elastic trial stress point $\boldsymbol{\sigma}_{n+1}^{trial}=\boldsymbol{\sigma}_n+\bar{\mathbf{D}}\left(\bar{K},\bar{G}\right):\Delta\boldsymbol{\varepsilon}_{n+1}$ is used as the initial iteration point. Selecting $\left\|\boldsymbol{\sigma}_n+\bar{\mathbf{D}}\left(\bar{K},\bar{G}\right):\Delta\boldsymbol{\varepsilon}_{n+1}\right\|^3$ as the value of c_{d} will save the computational cost and reduce the influence of the step size on the numerical stability to some extent.

4. Line search method

The solution of stress integral equations defined by Eq. (18) can be transformed into an unconstrained minimization problem shown below:

$$\min \quad \psi\left(\left\{\mathbf{x}\right\}\right)=\frac{1}{2}\left\{\mathbf{f}\left(\mathbf{x}\right)\right\}^T\left\{\mathbf{f}\left(\mathbf{x}\right)\right\} \tag{19}$$

where the subscript $n+1$ is omitted. The merit function ψ is a simple quadratic function of the nonlinear equations defined by Eq. (18). The solution of Eq. (18) is equivalent to the global minimum point of ψ. The iteration used to search the minimum point is defined by:

$$\left\{\mathbf{x}\right\}^{k+1}=\left\{\mathbf{x}\right\}^{k}+\alpha^k\left\{\mathbf{d}\right\}^{k} \tag{20}$$

where α^k and $\{\mathbf{d}\}^k$ are the step size and search direction vector at *k*th iteration, respectively. The Newton method is a usually good choice to determine search direction due to its asymptotically quadratic rate of convergence:

$$\{\mathbf{d}\}^k = -\left[\nabla\mathbf{f}(\mathbf{x})\right]_k^{-1}\{\mathbf{f}(\mathbf{x})\}^k \tag{21}$$

The task of the LSM is to optimize the step length α^k for a given search direction to achieve more reduction of the merit function. This gives rise to a new one-dimensional minimization problem about α^k:

$$\min \quad \psi(\alpha^k) = \frac{1}{2}\{\mathbf{f}(\alpha)\}_k^T\{\mathbf{f}(\alpha)\}^k \tag{22}$$

where $\{\mathbf{f}(\alpha)\}^k = \{\mathbf{f}(\mathbf{x}+\alpha\mathbf{d})\}^k$. The LSM will degenerate into the standard Newton method when α^k equals to 1. However, it is not easy to determine the optimal value of α^k by minimizing $\psi(\alpha^k)$ directly due to the fact that it will involve the computation of the Jacobian matrix. A more practical strategy is to minimize the approximation of $\psi(\alpha^k)$ to obtain an acceptable value of α^k that provides an adequate reduction in the merit function. Herein, a simple quadratic curve is used to fit $\psi(\alpha^k)$ as follows:

$$\hat{\psi}(\alpha^k) = A + B\alpha^k + C\alpha_k^2 \tag{23}$$

where the coefficient A, B, and C can be determined by substituting two points $(0,\ \psi(0))$ and $(\alpha_j^k,\ \psi(\alpha_j^k))$ into Eq. (23) and considering the condition $(0,\ \psi'(0))$, where $\psi'(0) = -2\psi(0)$. The quadratic approximation of $\psi(\alpha^k)$ is obtained as follows:

$$\hat{\psi}(\alpha^k) = (1 - 2\alpha^k + \alpha_k^2)\psi(0) + \alpha_k^2\psi(\alpha_j^k) \tag{24}$$

Minimizing Eq. (24), the following iterative formula is obtained to update α^k when the reduction of $\psi(\alpha^k)$ does not satisfy the requirements of the LSM:

$$\alpha_{j+1}^{k} = \frac{\psi(0)}{\psi(0) + 2\psi\left(\alpha_{j}^{k}\right)} \tag{25}$$

The same treatment can also be found in the literature (Scherzinger 2017; Yoon *et al.* 2020). Then, the upper limit of α^{k} is determined by *Goldstein's condition* (Nocedal & Wright 2006; Yoon *et al.* 2020) herein as follows:

$$\psi\left(\alpha_{j}^{k}\right) < \left(1 - 2\rho\alpha_{j}^{k}\right)\psi(0) \tag{26}$$

The lower limit of α^{k} is determined by the following expression to avoid having too small a step size (Pérez-Foguet & Armero 2002; Scherzinger 2017):

$$\alpha_{j+1}^{k} = \max\left\{\varsigma\alpha_{j}^{k}, \frac{\psi(0)}{\psi(0) + 2\psi\left(\alpha_{j}^{k}\right)}\right\} \tag{27}$$

where Pérez-Foguet & Armero (2002) proposed to use $\rho = 10^{-4}$ and $\varsigma = 0.1$. Eqs. (26) and (27) specify an interval for the acceptable values of α^{k}. Based on the LSM presented in this section and the unconstrained stress updating strategy presented in Section 2, the stress updating procedures of the MCC model are given in Fig. 4 where β is an input parameter. In theory, the smaller β, the closer the smooth curve is to the *KKT* condition. However, β cannot be too small to affect the numerical stability of floating-point calculation. In this paper, β is set to $FTOL^{2}/2$. This selection allows for a single step solution to be found. For example, the current step is the elastic loading, i.e., $\left\|\{\mathbf{f}\}_{n+1}^{0}\right\| = \sqrt{0^{2} + 0^{2} + 0^{2} + f_{4}^{2}} = \sqrt{f_{n+1}^{2} + FTOL^{2}} + f_{n+1}$. Then, the following inequality will hold: $\sqrt{f_{n+1}^{2} + FTOL^{2}} + f_{n+1} \le FTOL \quad \Rightarrow \quad f_{n+1}^{2} + FTOL^{2} \le f_{n+1}^{2} + FTOL^{2} - 2f_{n+1}FTOL \quad \Rightarrow$ $0 \le -2f_{n+1}FTOL$ due to $f_{n+1} < 0$ for the elastic step and $FTOL > 0$.

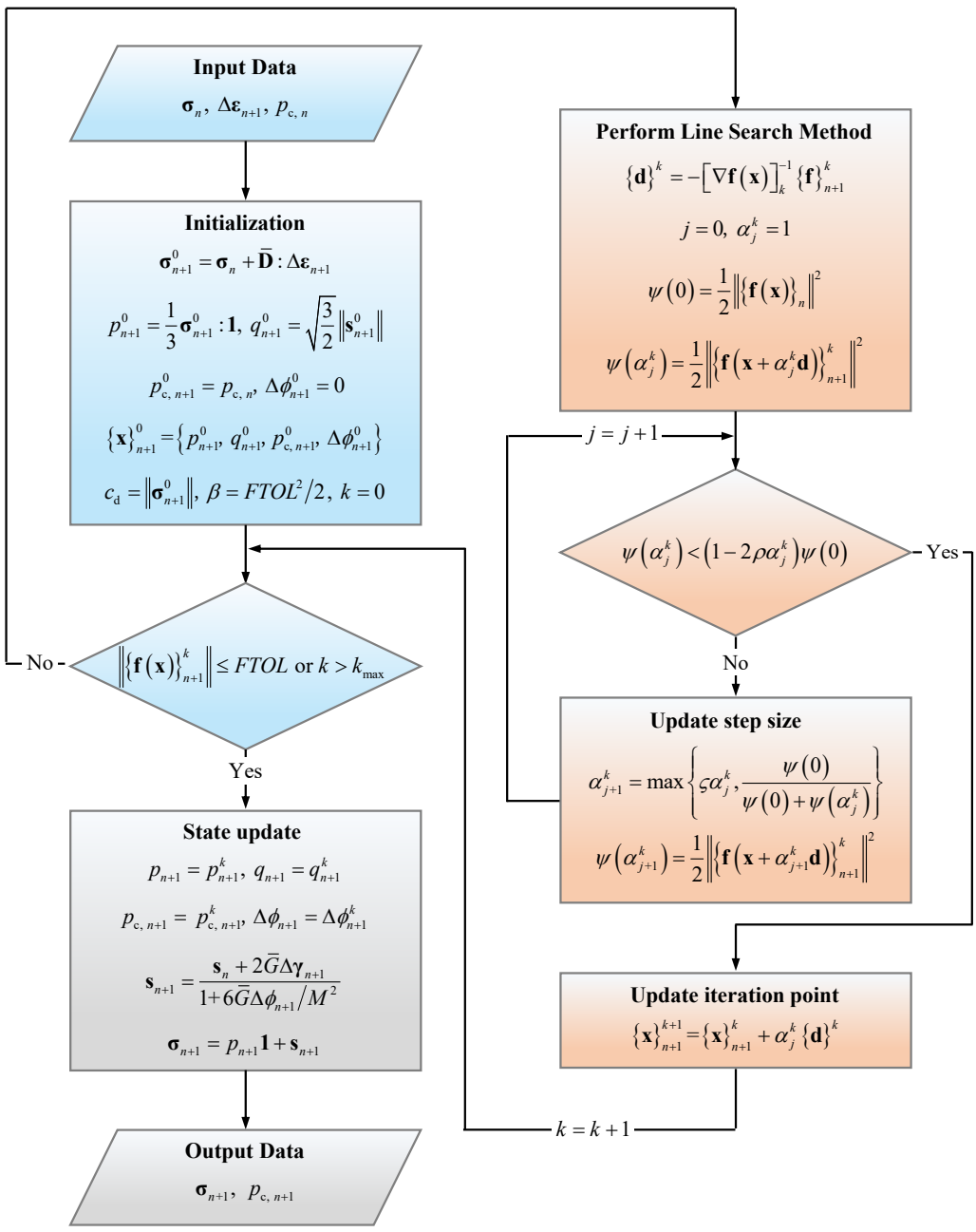

Fig. 4 Flow chart of unconstrained stress updating algorithm using the LSM.

In addition, a necessary emphasis is needed for the meaning of symbols *n*, *k*, and *j*, in which *n* denotes the incremental load step, *k* denotes the local stress updating iteration, and *j* denotes the number of iterations required to obtain the optimal search step size of the LSM. Finally, we provide a synopsis of the LSM used in this paper. First, $\alpha^k_0 = 1$ is used as the initial value of step size. If the condition Eq. (26) is satisfied, then we set $\{\mathbf{x}\}^{k+1} = \{\mathbf{x}\}^k + \alpha^k\{\mathbf{d}\}^k$. If α^k_j exceeds the upper

limit defined by Eq. (26), then we update α_{j+1}^{k} using Eq. (27) to search the acceptable value of step size.

5. Smoothing consistent tangent operator

In the local calculation of nonlinear finite element analysis, two things need to be done. One is to update the model's state variables using the stress update algorithm, and the other is to provide the CTO $\partial\boldsymbol{\sigma}_{n+1}/\partial\boldsymbol{\varepsilon}_{n+1}$ that is consistent with the integral equations of the model. In the global calculation, the updated state variables are used to determine the structural internal forces, while the CTO is used to generate the global stiffness of the structure. When the Newton method is employed to solve the equilibrium equations in the global calculation, the CTO can preserve the global solution's quadratic convergence speed (Wu *et al.* 2006). Based on the operator splitting stress updating strategy, the elastic and elastoplastic CTOs of the MCC model have been derived in the studies by Borja and his co-workers (Borja & Lee 1990; Borja 1991). In this section, the unconstrained stress updating strategy gives rise to a smoothing CTO with a unified form.

Taking the derivative of Eq. (17), we can obtain:

$$\frac{\partial\boldsymbol{\sigma}_{n+1}}{\partial\boldsymbol{\varepsilon}_{n+1}} = \mathbf{1}\otimes\frac{\partial p_{n+1}}{\partial\boldsymbol{\varepsilon}_{n+1}} + \frac{\partial\mathbf{s}_{n+1}}{\partial\boldsymbol{\varepsilon}_{n+1}} \tag{28}$$

where $\partial p_{n+1}/\partial\boldsymbol{\varepsilon}_{n+1}$ is expressed by:

$$\frac{\partial p_{n+1}}{\partial\boldsymbol{\varepsilon}_{n+1}} = K_{n+1}\left[\mathbf{1} - \Delta\phi_{n+1}\left(2\frac{\partial p_{n+1}}{\partial\boldsymbol{\varepsilon}_{n+1}} - \frac{\partial p_{\mathrm{c},\,n+1}}{\partial\boldsymbol{\varepsilon}_{n+1}}\right) - \left(2p_{n+1} - p_{\mathrm{c},\,n+1}\right)\frac{\partial\Delta\phi_{n+1}}{\partial\boldsymbol{\varepsilon}_{n+1}}\right] \tag{29}$$

where

$$\frac{\partial p_{\mathrm{c},\,n+1}}{\partial\boldsymbol{\varepsilon}_{n+1}} = p_{\mathrm{c},\,n+1}c_{\mathrm{p}}\left[\Delta\phi_{n+1}\left(2\frac{\partial p_{n+1}}{\partial\boldsymbol{\varepsilon}_{n+1}} - \frac{\partial p_{\mathrm{c},\,n+1}}{\partial\boldsymbol{\varepsilon}_{n+1}}\right) + \left(2p_{n+1} - p_{\mathrm{c},\,n+1}\right)\frac{\partial\Delta\phi_{n+1}}{\partial\boldsymbol{\varepsilon}_{n+1}}\right] \tag{30}$$

$$K_{n+1} = c_{\kappa}p_{n}\exp\left\{c_{\kappa}\left[\Delta\varepsilon_{\mathrm{v},\,n+1} - \Delta\phi_{n+1}\left(2p_{n+1} - p_{\mathrm{c},\,n+1}\right)\right]\right\} \tag{31}$$

From Eqs. (29) and (30), the expressions of $\partial p_{n+1}/\partial \boldsymbol{\varepsilon}_{n+1}$ and $\partial p_{\mathrm{c},\,n+1}/\partial \boldsymbol{\varepsilon}_{n+1}$ can be simplified as the function of $\partial \Delta\phi_{n+1}/\partial \boldsymbol{\varepsilon}_{n+1}$ as follows:

$$\frac{\partial p_{n+1}}{\partial \boldsymbol{\varepsilon}_{n+1}} = a_1 K_{n+1}\mathbf{1} + a_2 K_{n+1}\frac{\partial \Delta\phi_{n+1}}{\partial \boldsymbol{\varepsilon}_{n+1}} \tag{32}$$

$$\frac{\partial p_{\mathrm{c},\,n+1}}{\partial \boldsymbol{\varepsilon}_{n+1}} = a_3 K_{n+1}\mathbf{1} + a_4 K_{n+1}\frac{\partial \Delta\phi_{n+1}}{\partial \boldsymbol{\varepsilon}_{n+1}} \tag{33}$$

where the coefficients a_1, a_2, a_3, and a_4 are expressed by:

$$\begin{cases} a_0 = 1 + p_{\mathrm{c},\,n+1} c_{\mathrm{p}} \Delta\phi_{n+1} + 2\Delta\phi_{n+1} K_{n+1} \\ a_1 = \left(1 + p_{\mathrm{c},\,n+1} c_{\mathrm{p}} \Delta\phi_{n+1}\right)/a_0 \\ a_2 = -\left(2p_{n+1} - p_{\mathrm{c},\,n+1}\right)/a_0 \\ a_3 = 2p_{\mathrm{c},\,n+1} c_{\mathrm{p}} \Delta\phi_{n+1}/a_0 \\ a_4 = p_{\mathrm{c},\,n+1} c_{\mathrm{p}} \left(2p_{n+1} - p_{\mathrm{c},\,n+1}\right)/\left(a_0 K_{n+1}\right) \end{cases} \tag{34}$$

Taking the derivative of Eq. (15) with respect to $\boldsymbol{\varepsilon}_{n+1}$, $\partial \mathbf{s}_{n+1}/\partial \boldsymbol{\varepsilon}_{n+1}$ can be also written as the function of $\partial \Delta\phi_{n+1}/\partial \boldsymbol{\varepsilon}_{n+1}$ as follows:

$$\frac{\partial \mathbf{s}_{n+1}}{\partial \boldsymbol{\varepsilon}_{n+1}} = 2\bar{G}a_5\left[\mathbf{P} + \frac{\Delta\boldsymbol{\gamma}_{n+1}}{\bar{G}} \otimes \frac{rK_{n+1} - \bar{G}}{\Delta\varepsilon^{\mathrm{e}}_{\mathrm{v},\,n+1}}\left(a_1\mathbf{1} + a_2\frac{\partial \Delta\phi_{n+1}}{\partial \boldsymbol{\varepsilon}_{n+1}}\right)\right] - \frac{2\sqrt{6}q\bar{G}a_5}{M^2}\hat{\mathbf{n}} \otimes \left[\frac{\partial \Delta\phi_{n+1}}{\partial \boldsymbol{\varepsilon}_{n+1}} + \frac{\Delta\phi_{n+1}}{\bar{G}}\frac{rK_{n+1} - \bar{G}}{\Delta\varepsilon^{\mathrm{e}}_{\mathrm{v},\,n+1}}\left(a_1\mathbf{1} + a_2\frac{\partial \Delta\phi_{n+1}}{\partial \boldsymbol{\varepsilon}_{n+1}}\right)\right] \tag{35}$$

where $a_5 = \left(1 + 6\bar{G}\Delta\phi_{n+1}/M^2\right)^{-1}$. $\mathbf{P} = \mathbf{I} - \mathbf{1} \otimes \mathbf{1}/3$ is the fourth-order projection tensor where $\mathbf{I}$ is the fourth-order unit. $\hat{\mathbf{n}} = \mathbf{s}_{n+1}/\|\mathbf{s}_{n+1}\|$. Now, only $\partial \Delta\phi_{n+1}/\partial \boldsymbol{\varepsilon}_{n+1}$ is unknown, which can be obtained by imposing the total differential of Eq. $(18)_4$:

$$\frac{\partial f_4}{\partial f}\left[\frac{3\mathbf{s}_{n+1}}{M^2} : \frac{\partial \mathbf{s}_{n+1}}{\partial \boldsymbol{\varepsilon}_{n+1}} + \left(2p_{n+1} - p_{\mathrm{c},\,n+1}\right)\frac{\partial p_{n+1}}{\partial \boldsymbol{\varepsilon}_{n+1}} - p_{n+1}\frac{\partial p_{\mathrm{c},\,n+1}}{\partial \boldsymbol{\varepsilon}_{n+1}}\right] + \frac{\partial f_4}{\partial \Delta\phi_{n+1}}\frac{\partial \Delta\phi_{n+1}}{\partial \boldsymbol{\varepsilon}_{n+1}} = 0 \tag{36}$$

Then, substituting Eqs. (32), (33), and (35) into Eq. (36) and rearranging the expression can yield:

$$\frac{\partial \Delta\phi_{n+1}}{\partial \boldsymbol{\varepsilon}_{n+1}} = b_1\mathbf{1} + b_2\hat{\mathbf{n}} \tag{37}$$

where

$$
\begin{cases}
b_0 = \chi_0 \left\{ \left[\left(\dfrac{\hat{\mathbf{n}}}{\sqrt{6}} : \Delta\boldsymbol{\gamma}_{n+1} - \dfrac{q\Delta\phi_{n+1}}{M^2} \right) a_2 \dfrac{rK_{n+1} - \bar{G}}{\Delta\varepsilon^{\mathrm{e}}_{\mathrm{v},\,n+1}} - \dfrac{q\bar{G}}{M^2} \right] \dfrac{12qa_5}{M^2} + \left[\left(2a_2 - a_4\right) p_{n+1} - a_2 p_{\mathrm{c},\,n+1} \right] K_{n+1} \right\} + \chi_1 \\
b_1 = -\chi_0 \left[\left(\dfrac{\hat{\mathbf{n}}}{\sqrt{6}} : \Delta\boldsymbol{\gamma}_{n+1} - \dfrac{q\Delta\phi_{n+1}}{M^2} \right) \dfrac{12qa_1a_5}{M^2} \dfrac{rK_{n+1} - \bar{G}}{\Delta\varepsilon^{\mathrm{e}}_{\mathrm{v},\,n+1}} + \left(2a_1 - a_3\right) p_{n+1} K_{n+1} - a_1 p_{\mathrm{c},\,n+1} K_{n+1} \right] \Big/ b_0 \\
b_2 = -\chi_0 \dfrac{2\sqrt{6}q\bar{G}a_5}{M^2} \Big/ b_0
\end{cases}
\tag{38}
$$

where

$$
\begin{cases}
\chi_0 = \dfrac{\partial f_4}{\partial f_{n+1}} = \dfrac{f_{n+1}}{\sqrt{\left(c_{\mathrm{d}}\Delta\phi_{n+1}\right)^2 + f_{n+1}^2 + 2\beta}} + 1 \\
\chi_1 = \dfrac{\partial f_4}{\partial \Delta\phi_{n+1}} = \dfrac{c_{\mathrm{d}}^2 \Delta\phi_{n+1}}{\sqrt{\left(c_{\mathrm{d}}\Delta\phi_{n+1}\right)^2 + f_{n+1}^2 + 2\beta}} - c_{\mathrm{d}}
\end{cases}
\tag{39}
$$

Substituting Eqs. (32), (35) and (37) into Eq. (28), the smoothing CTO based on the unconstrained stress updating strategy is obtained:

$$
\begin{aligned}
\frac{\partial\boldsymbol{\sigma}_{n+1}}{\partial\boldsymbol{\varepsilon}_{n+1}} = {} & 2\bar{G}a_5\mathbf{P} + \left(a_1 + a_2 b_1\right) K_{n+1}\mathbf{1}\otimes\mathbf{1} + a_2 b_2 K_{n+1}\mathbf{1}\otimes\hat{\mathbf{n}} + 2a_5 \frac{rK_{n+1} - \bar{G}}{\Delta\varepsilon^{\mathrm{e}}_{\mathrm{v},\,n+1}} \left(a_1 + a_2 b_1\right) \Delta\boldsymbol{\gamma}_{n+1}\otimes\mathbf{1} + 2a_2 a_5 b_2 \frac{rK_{n+1} - \bar{G}}{\Delta\varepsilon^{\mathrm{e}}_{\mathrm{v},\,n+1}} \Delta\boldsymbol{\gamma}_{n+1}\otimes\hat{\mathbf{n}} \\
& - \frac{2\sqrt{6}qa_5}{M^2} \left[b_1\bar{G} + \frac{\left(rK_{n+1} - \bar{G}\right)\Delta\phi_{n+1}}{\Delta\varepsilon^{\mathrm{e}}_{\mathrm{v},\,n+1}} \left(a_1 + a_2 b_1\right) \right] \hat{\mathbf{n}}\otimes\mathbf{1} - \frac{2\sqrt{6}qa_5}{M^2} \left(b_2\bar{G} + a_2 b_2 \frac{\left(rK_{n+1} - \bar{G}\right)\Delta\phi_{n+1}}{\Delta\varepsilon^{\mathrm{e}}_{\mathrm{v},\,n+1}} \right) \hat{\mathbf{n}}\otimes\hat{\mathbf{n}}
\end{aligned}
\tag{40}
$$

It can be seen that the smoothing CTO does not distinguish between the elastic and elastoplastic loading cases due to the fact that the integral equations of the constitutive model are a set of smooth equations without loading/unloading inequality constraints. In addition, when β trends to 0, the smoothing CTO can degenerate into the elastic and plastic CTOs derived by the operator splitting technique in elastic and elastoplastic loading cases, respectively. For the elastoplastic loading case, there are $\Delta\phi_{n+1} > 0$ and $f_{n+1} = 0$ when β tends to be 0. Then, the results that $\chi_0 = 0 + 1 = 1$ and $\chi_1 = c_{\mathrm{d}} - c_{\mathrm{d}} = 0$ can be obtained. Substituting $\chi_0 = 1$ and $\chi_1 = 0$ into Eq. (36), Eq. (36) will be reduced to the total differential of the yield function. The derivation of smoothing CTO will thus yield the same result as the plastic CTO.

Before proving that the smoothing CTO can also degenerate into the elastic CTO under the condition of elastic loading/unloading, the expression of the elastic CTO of the MCC model is derived first. Considering the integral equations of the stress tensor in elastic loading case under the operator splitting stress updating strategy, we have:

$$\boldsymbol{\sigma}_{n+1}=\left(p_n\mathbf{1}+\mathbf{s}_n\right)+\left(\bar{K}\Delta\varepsilon_{\mathrm{v},\,n+1}\mathbf{1}+2\bar{G}\Delta\boldsymbol{\gamma}_{n+1}\right) \tag{41}$$

Taking Eq. (41) with respect to $\boldsymbol{\varepsilon}_{n+1}$, the elastic CTO can be obtained as follow:

$$\frac{\partial\boldsymbol{\sigma}_{n+1}}{\partial\boldsymbol{\varepsilon}_{n+1}}=\Delta\varepsilon_{\mathrm{v},\,n+1}\frac{\left(K_{n+1}-\bar{K}\right)}{\Delta\varepsilon_{\mathrm{v},\,n+1}}\frac{\partial\Delta\varepsilon_{\mathrm{v},\,n+1}}{\partial\boldsymbol{\varepsilon}_{n+1}}\otimes\mathbf{1}+\bar{K}\frac{\partial\Delta\varepsilon_{\mathrm{v},\,n+1}}{\partial\boldsymbol{\varepsilon}_{n+1}}\mathbf{1}+2\frac{\left(rK_{n+1}-\bar{G}\right)}{\Delta\varepsilon_{\mathrm{v},\,n+1}}\Delta\boldsymbol{\gamma}_{n+1}\otimes\frac{\partial\Delta\varepsilon_{\mathrm{v},\,n+1}}{\partial\boldsymbol{\varepsilon}_{n+1}}+2\bar{G}\frac{\partial\Delta\boldsymbol{\gamma}_{n+1}}{\partial\boldsymbol{\varepsilon}_{n+1}} \tag{42}$$

Substituting $\partial\Delta\varepsilon_{\mathrm{v},\,n+1}/\partial\boldsymbol{\varepsilon}_{n+1}=\mathbf{1}$ and $\partial\Delta\boldsymbol{\gamma}_{n+1}/\partial\boldsymbol{\varepsilon}_{n+1}=\mathbf{P}$ into Eq. (42), the expression of the elastic CTO is given as follows:

$$\frac{\partial\boldsymbol{\sigma}_{n+1}}{\partial\boldsymbol{\varepsilon}_{n+1}}=K_{n+1}\mathbf{1}\otimes\mathbf{1}+2\bar{G}\mathbf{P}+2\frac{\left(rK_{n+1}-\bar{G}\right)}{\Delta\varepsilon_{\mathrm{v},\,n+1}}\Delta\boldsymbol{\gamma}_{n+1}\otimes\mathbf{1} \tag{43}$$

Now, we give the degradation form of the smoothing CTO in the elastic loading case. For the elastic load step, there are $\Delta\phi_{n+1}=0$ and $f_{n+1}<0$ when β tends to be 0. Substituting $\Delta\phi_{n+1}=0$ and $f_{n+1}<0$ into Eq. (39), the results that $\chi_0=-1+1=0$ and $\chi_1=0-c_{\mathrm{d}}=-c_{\mathrm{d}}$ are obtained, and then substituting them into Eq. (36), we can obtain $\partial\Delta\phi_{n+1}/\partial\boldsymbol{\varepsilon}_{n+1}=0$. Substituting $\partial\Delta\phi_{n+1}/\partial\boldsymbol{\varepsilon}_{n+1}=0$ and $\Delta\phi_{n+1}=0$ into Eq. (32), we obtain:

$$\frac{\partial p_{n+1}}{\partial\boldsymbol{\varepsilon}_{n+1}}=K_{n+1}\mathbf{1} \tag{44}$$

Similarly, substituting $\partial\Delta\phi_{n+1}/\partial\boldsymbol{\varepsilon}_{n+1}=0$ and $\Delta\phi_{n+1}=0$ into Eq. (35), we obtain:

$$\frac{\partial\mathbf{s}_{n+1}}{\partial\boldsymbol{\varepsilon}_{n+1}}=2\bar{G}\mathbf{P}+\frac{2\left(rK_{n+1}-\bar{G}\right)}{\Delta\varepsilon^{\mathrm{e}}_{\mathrm{v},\,n+1}}\Delta\boldsymbol{\gamma}_{n+1}\otimes\mathbf{1} \tag{45}$$

Substituting Eqs. (44) and (45) into Eq. (28), we have:

$$\frac{\partial\boldsymbol{\sigma}_{n+1}}{\partial\boldsymbol{\varepsilon}_{n+1}}=K_{n+1}\mathbf{1}\otimes\mathbf{1}+2\bar{G}\mathbf{P}+\frac{2\left(rK_{n+1}-\bar{G}\right)}{\Delta\varepsilon^{\mathrm{e}}_{\mathrm{v},\,n+1}}\Delta\boldsymbol{\gamma}_{n+1}\otimes\mathbf{1} \tag{46}$$

Considering the condition that there is $\Delta\varepsilon^{\mathrm{e}}_{\mathrm{v},\,n+1}=\Delta\varepsilon_{\mathrm{v},\,n+1}$ for the elastic load step, the

degradation form of the smoothing CTO defined by Eq. (46) is equivalent to the elastic CTO defined by Eq. (43). The above equivalences also prove the rationality using the smoothing function instead of the *KKT* conditions.

6. Numerical validation

Based on the proposed algorithm, the MCC model was implemented in ABAQUS finite element software via the external subroutine UMAT, which was then used to simulate four boundary value problems encompassing the typical load conditions of geotechnical engineering. In the first boundary problem, the correctness of the proposed algorithm is validated by comparing it with the analytical solution. In the following three examples, the computational efficiency and robustness of the proposed algorithm are explored by comparing with the ABAQUS/Standard DIM, i.e., implicit return mapping algorithm (Simo & Hughes 2006). In addition, all the examples are run on the same computer, which is outfitted with an Intel Core i7-9750 processor @ 2.60 GHz, 16 GB of RAM.

6.1. Cylindrical cavity expansion

First, the proposed algorithm is compared with the analytical solution of the cylindrical cavity expansion problem provided by the literature (Chen & Abousleiman 2012; Chen & Abousleiman 2013) for both undrained and drained conditions. As shown in Fig. 5 (a), a cylindrical cavity with the initial radius r_0 exists in a cylindrical soil with infinite height and radius, which is subjected to initial total vertical stress σ_{v0}, horizontal stress σ_{h0} and internal pressure σ_0. Then, under the action of internal pressure, the radius of the cylindrical cavity gradually expands from r_0 to r_1. As can be noticed, the cylindrical cavity expansion is an axisymmetric plane strain problem, which can be analyzed by the simplified model shown in Fig. 5 (b). The geometric simplification can be implemented by using the eight nodes axisymmetric pore pressure element (CAX8P) for the undrained case and the eight nodes axisymmetric element (CAX8) for the drained, respectively.

Table 1 presents the material parameters of the soil from the literature (Chen & Abousleiman 2012) where the OCR, K_0 and e_1 denote the overconsolidation ratio, the coefficient of earth pressure at rest, and the void ratio at $p = 1\ \text{kPa}$ respectively. The simulation process includes three analysis steps. In the initial step, the translational degree of freedom of the top and bottom edges in the 3-direction and the translational degree of freedom of the left edge in the 1-direction are fixed. The translational degree of freedom of the right edge in the 1-direction is fixed only for the drained case. In the geostatic step, the pressure load is applied on the right edge of the model to balance the in-situ stress. In the third analysis step, the displacement load in the 1-direction is applied on the left edge of the model to simulate the cavity expansion process. It is worth noting that, for the undrained case, the permeability coefficient and the total time of the third analysis step are set to 2.3×10^{-3} and 0.001 s (Liu *et al.* 2019). It can be approximately considered that there is almost no dissipation of pore water pressure in the cavity expansion process due the very short drainage time. The initial pore water pressure is set to $u_p = 0\ \text{kPa}$. Fig. 6 and Fig. 7 show the comparison results for the undrained and drained conditions, respectively. The changes law of the axial stress σ'_r, the radial stress σ'_θ, the vertical stresses σ'_z, the excess pore water pressure Δu_p and the specific volume v from the proposed algorithm and the analytical solution are in good agreement, which proves the correctness of the proposed algorithm and the effectiveness of the UMAT.

Table 1 Summary of soil properties

OCR	σ'_{r0}	$\sigma'_{\theta0}$	σ'_{z0}	p'_0	q'_0	e_0	K_0
1	100	100	160	120	60	1.086	0.625
3	120	120	120	120	0	0.973	1.0
10	144	144	72	120	72	0.802	2.0
$M = 1.2$, $\lambda = 0.15$, $\kappa = 0.03$, $\nu = 0.278$, $e_1 = 1.823$							

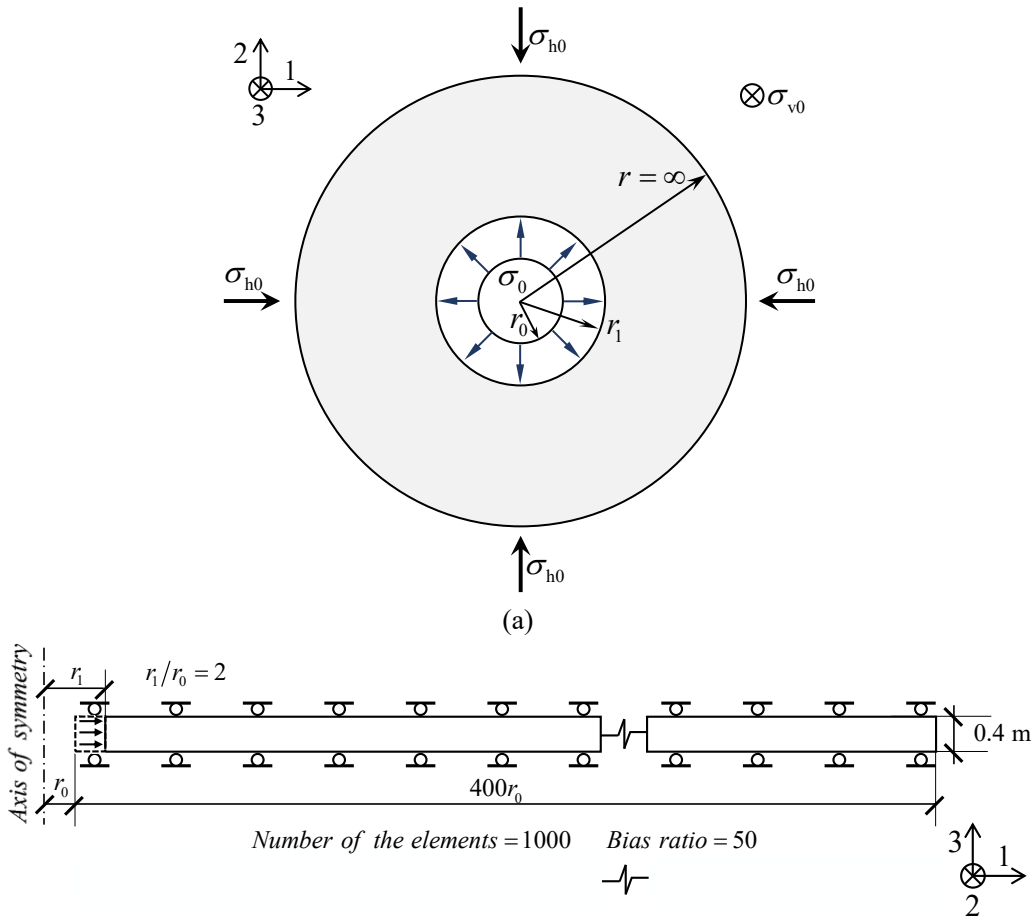

Fig. 5 Summary of cylindrical cavity expansion: (a) original boundary problem; (b) simplified model and mesh.

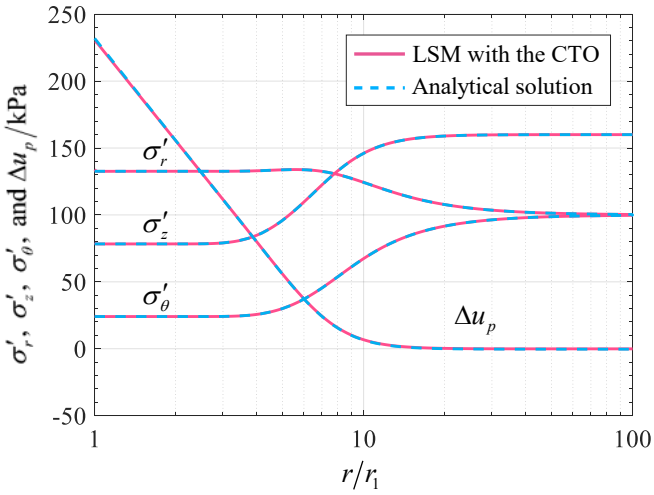

(a)

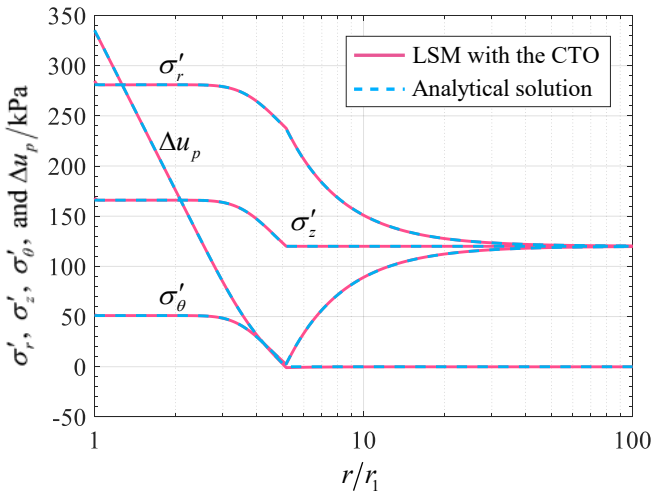

(b)

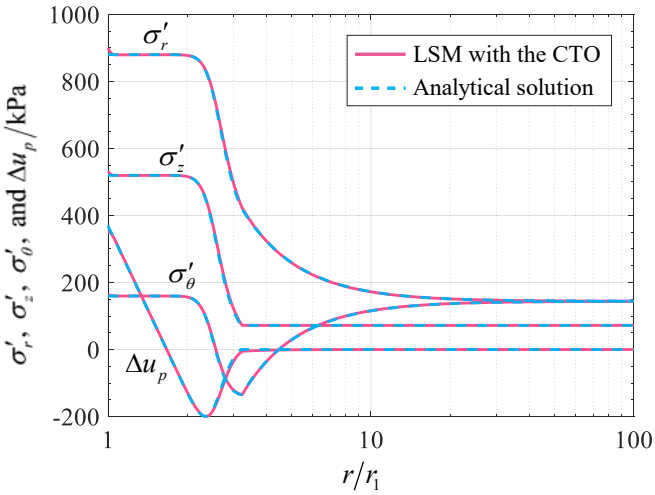

(c)

Fig. 6 Comparison between the proposed algorithm and analytical solution under undrained conditions: (a) OCR = 1; (b) OCR = 3; (c) OCR = 10.

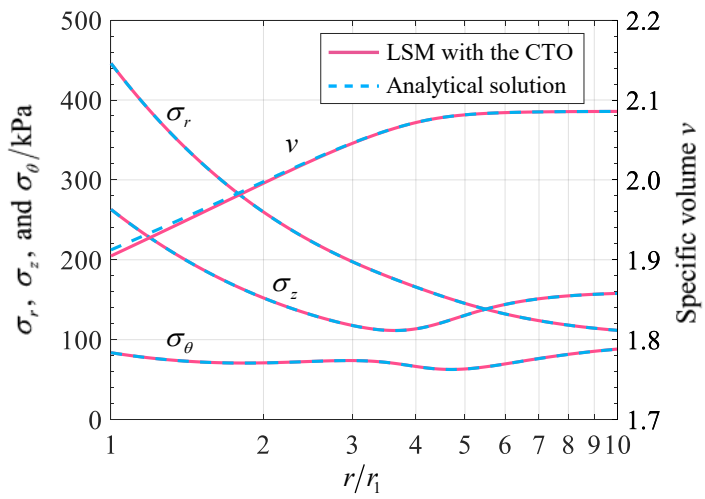

(a)

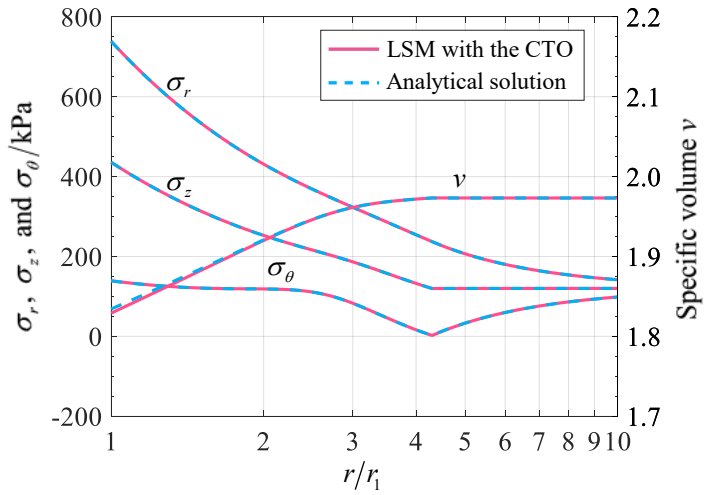

(b)

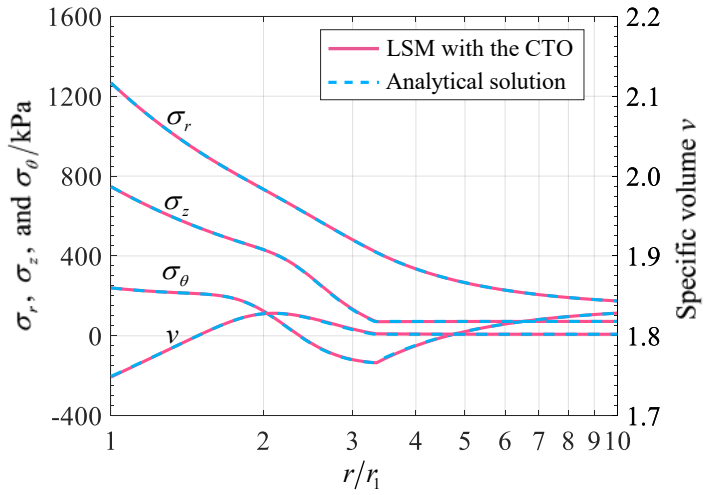

(c)

Fig. 7 Comparison between the proposed algorithm and analytical solution under drained conditions: (a) OCR = 1; (b) OCR = 3; (c) OCR = 10.

6.2. Tunnel excavation

Tunnel excavation simulation is a typical application for the MCC model in the numerical analysis of geotechnical engineering (Gawecka *et al.* 2021). This subsection considers a numerical example of tunnel excavation with lining support. The geometry and mesh of the numerical model are presented in Fig. 8. The element type of soil and lining is the 20 nodes brick element (C3D20). The material parameters of the MCC model and the unit weight γ_w of soil are set to $M = 1.2$, $\lambda = 0.2$, $\kappa = 0.04$, $\nu = 0.35$, $e_1 = 2$, and $\gamma_w = 20\ \mathrm{kN/m^3}$, respectively. The initial stress field

and initial void ratio e_0 , which change along the depth of soil layer, are generated in the geostatic stress analysis step, where $e_0 = e_1 - \lambda \ln(p_0) + \kappa \ln(p_0/p)$ based on the critical state soil mechanics. In the excavation analysis step, the removal of soil and the addition of lining are realized based on the element activation and deactivation, respectively. The simulation results of tunnel excavation are shown in Fig. 9. It can be seen that resilience occurs at the tunnel's bottom and subsidence occurs at the tunnel's top, reflecting the deformation features of excavation in clay. The ground surface settlement is the greatest in the tunnel region due to soil removal, and it decreases with increasing horizontal distance, as shown in Fig. 9 (b). The ground surface settlement curve from the proposed algorithm is coincident with that from the ABAQUS/Standard DIM, which further verifies the correctness of the proposed algorithm and subroutine.

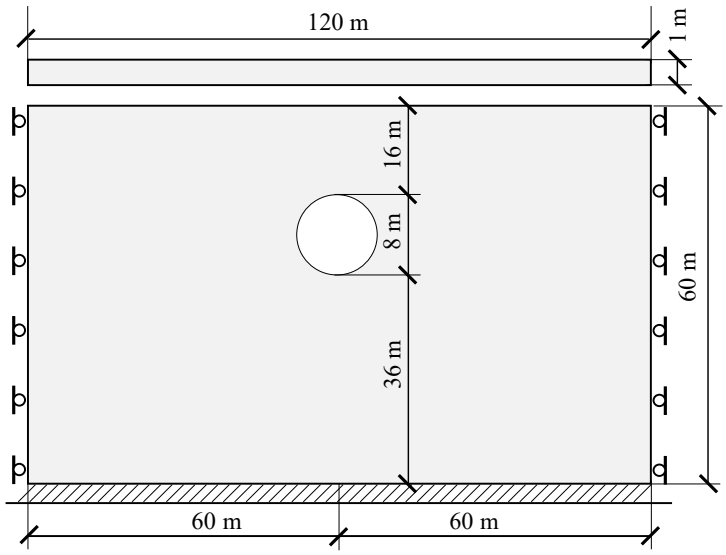

(a)

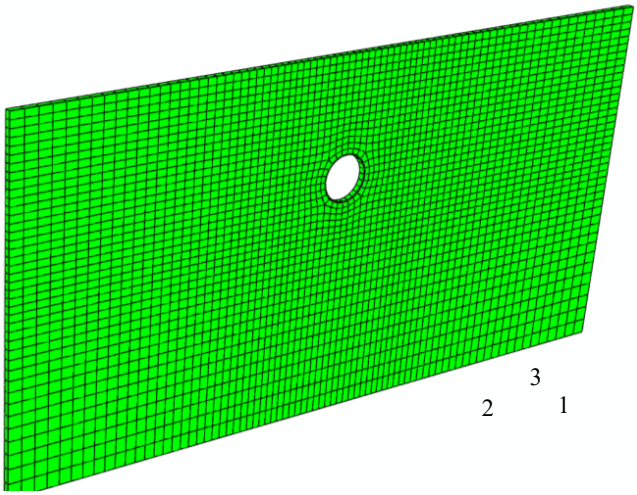

(b)

Fig. 8 Summary of tunnel excavation: (a) geometry and boundary conditions; (b) mesh.

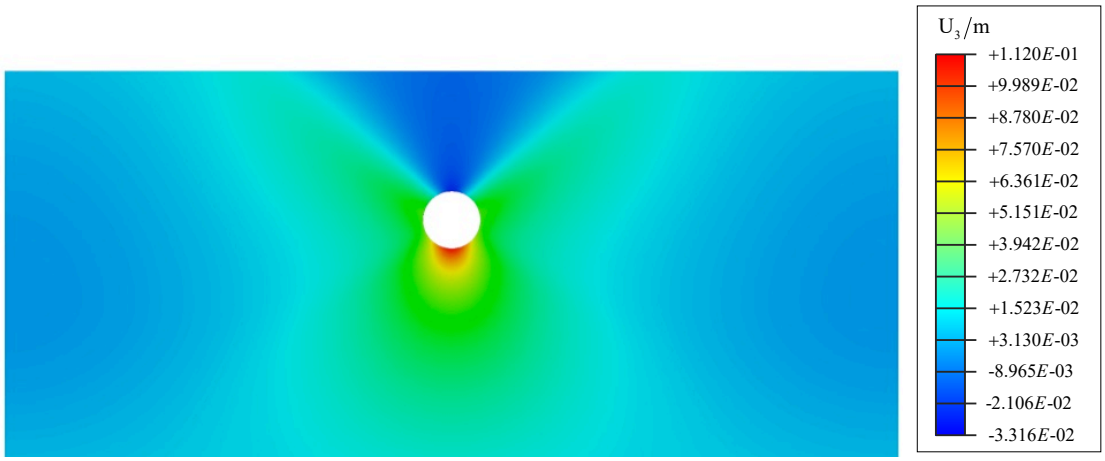

(a)

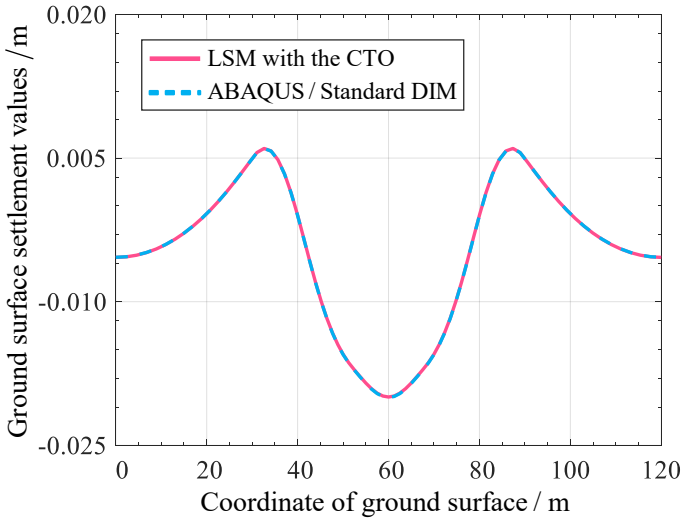

(b)

Fig. 9 Simulation results of tunnel excavation: (a) displacement field in the 3-direction; (b) ground surface settlement curves.

6.3. Bearing capacity test of the foundation

The following numerical example is a bearing capacity test of rigid strip footing, which has been widely used to assess the numerical implementation of critical state models due to the strong rotation of principal stress and the singularity at the edge of footing (Sheng *et al.* 2000). The geometric information, boundary conditions, and mesh of foundation are shown in Fig. 10, where the element type is set to 8 nodes brick element (C3D8). The elements 4 and 2260 at the edge of footing are indicated additionally for subsequent analysis. The material parameters of the MCC model and the unit weight γ_{w} of soil are taken from the literature (Sheng *et al.* 2000), i.e., $M = 0.898$, $\kappa = 0.05$, $\lambda = 0.25$, $\nu = 0.3$, $e_1 = 1.6$, and $\gamma_{\mathrm{w}} = 6\ \mathrm{kN/m^3}$. The initial stress field and initial void ratio e_0 are generated by the submerged weight of soil and pre-load $50\ \mathrm{kPa}$ imposed on the ground surface in the geostatic stress balance analysis. In the unload analysis step, the pre-load is completely removed with 4 equal load increments. Then, the displacement with $\mathrm{U}_3 = -0.15\mathrm{m}$ is applied on the footing in the load analysis step with 16 equal load increments. Fig. 11 (a) presents the generalized shear stress distribution of the soil layer at the end of the load. In Fig. 11 (b), the load-displacement responses from the LSM and ABAQUS/Standard DIM are in good agreement. The reasonability of the proposed algorithm is validated once again. Notes that the continuum tangent operator is also considered in the implementation of the MCC model to highlight the effectiveness of the smoothing CTO for the convergence behaviour of the global solution.

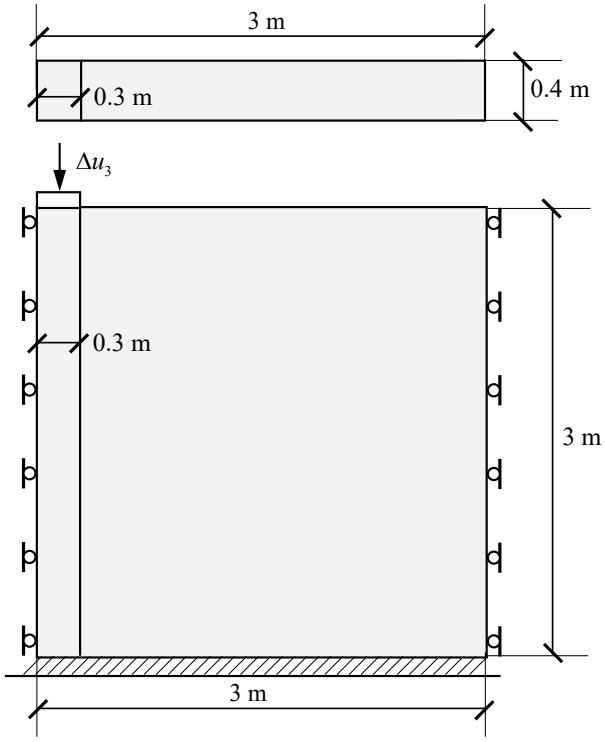

(a)

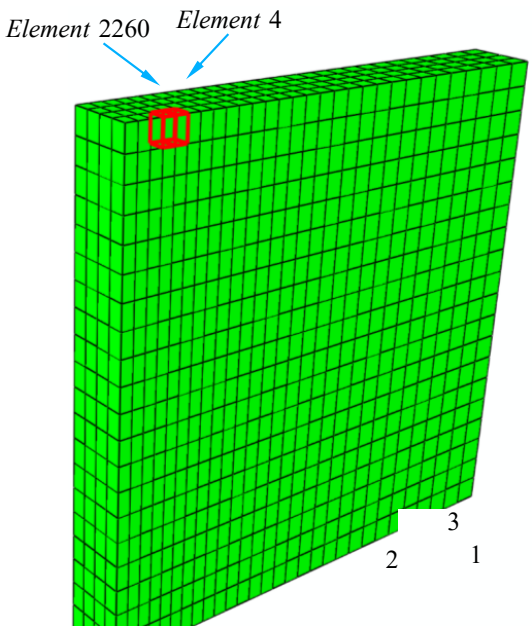

(b)

Fig. 10 Summary of bearing capacity test of foundation: (a) geometry and boundary conditions; (b) mesh.

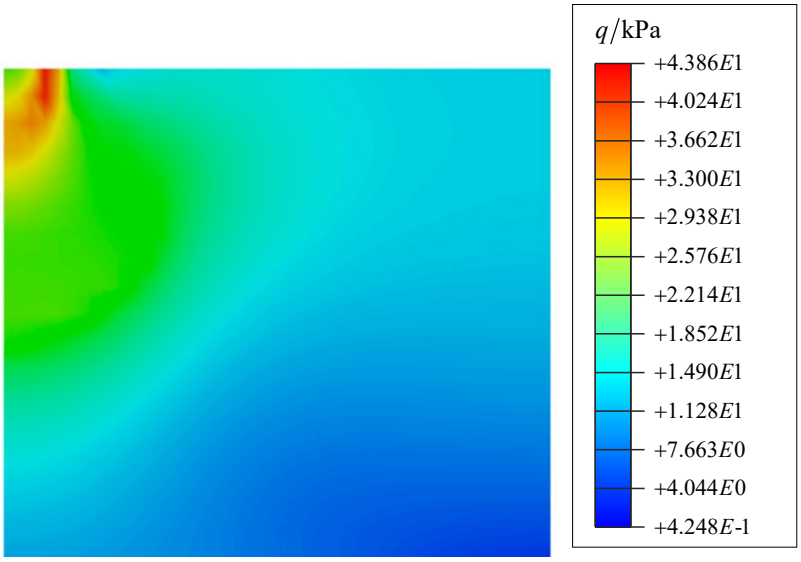

(a)

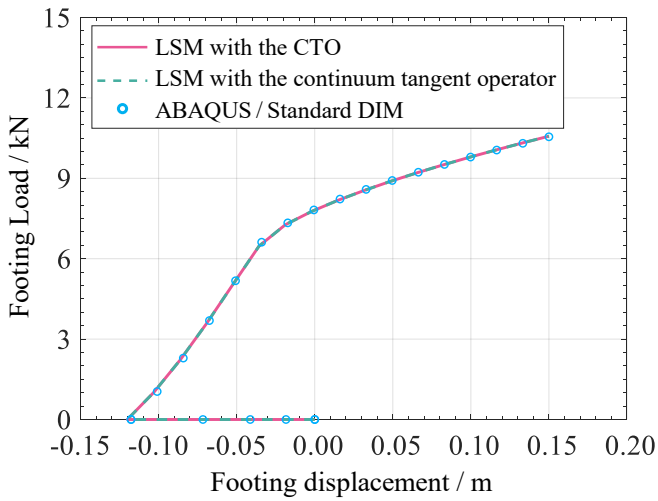

(b)

Fig. 11 Simulation results of bearing capacity test of foundation: (a) generalized shear stress distribution; (b) footing load versus footing displacement.

The convergence behaviour at the critical node for different algorithms is depicted in Fig. 12. In comparison to the LSM with the continuum tangent operator, the LSM with the CTO and ABAQUS/Standard DIM shows excellent convergence. The reason is that the CTO can guarantee the quadratic convergence speed of the Newton method used in the global equilibrium problem. Using the continuum tangent operator instead of the CTO will disturb the search direction of the Newton method and further destroy the convergence speed and radius of the Newton method.

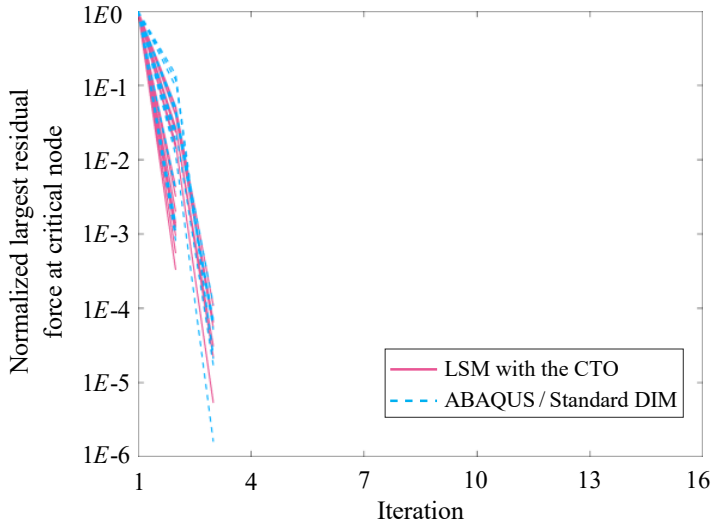

(a)

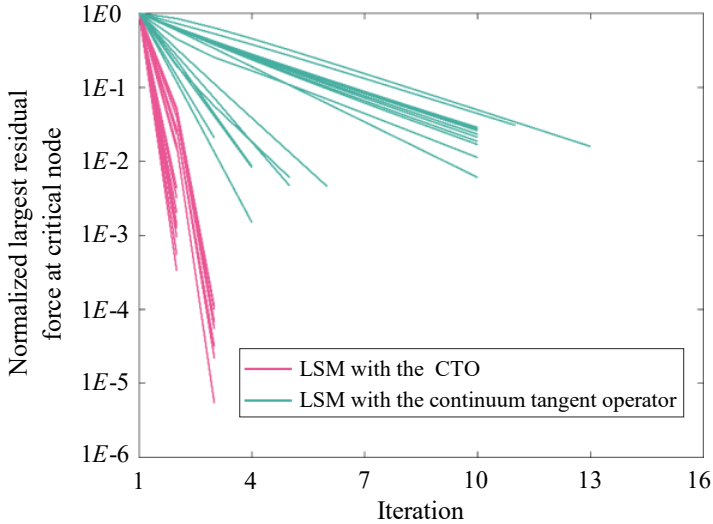

(b)

Fig. 12 Convergence behaviour at the critical node: (a) LSM with the CTO and the ABAQUS/Standard DIM; (b) LSM with the CTO and the continuum tangent operator.

Similar results are also observed in Fig. 13. For the LSM with CTO and ABAQUS/Standard DIM, the overall number of iterations and the CPU time consumed are similar. This high similarity of convergence speed also verifies the validity of smoothing CTO derived by the unconstrained stress updating strategy. For the LSM with the continuum tangent operator, three to four times the iteration number and computation time are required, significantly increasing the computational cost of numerical analysis. On the other hand, it is worth emphasizing that the LSM will require some

additional computational efforts for the determination of the optimal step size compared with the Newton method. This additional computational cost will lead to an increase of about 5% in computing time compared with the Newton method (Lester & Scherzinger 2017) when the number of global equilibrium iteration is the same. The main advantage of the LSM is to allow larger step size calculation.

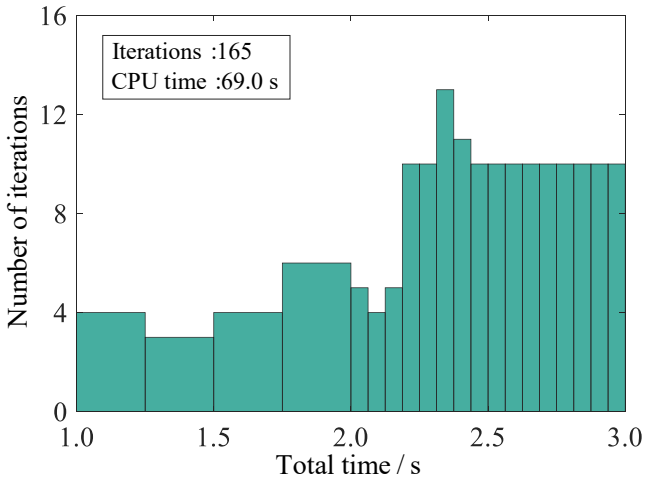

(a)

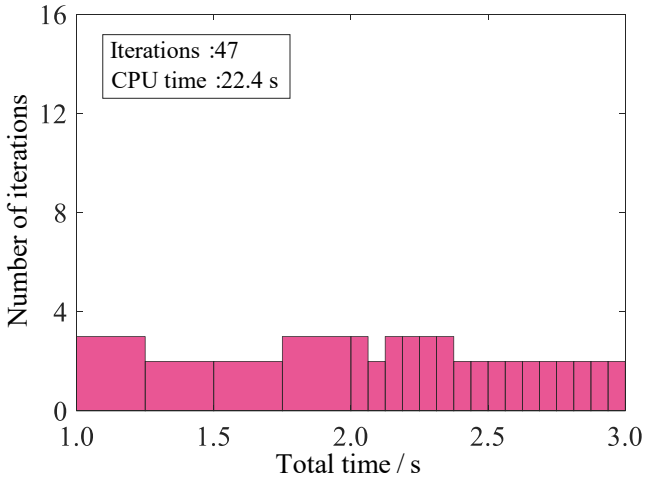

(b)

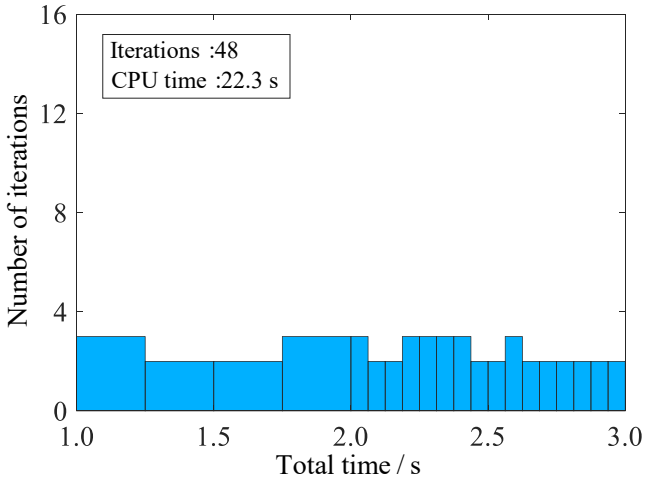

(c)

Fig. 13 Number of iterations at each load increment: (a) LSM with the continuum tangent operator; (b) LSM with the CTO; (c) ABAQUS/Standard DIM.

In what follows, the evolution of stress state and yield surface corresponding to elements 4 and 2260 in Fig. 10 (b) are analyzed, which will aid knowledge of the unconstrained stress updating strategy. Note that, in both elements, only integral point 8 is employed. In the unloading analysis step, i.e., the path from stress point 1 to stress point 5, the stress points of the two elements break away from the yield surface and move in the elastic region, as shown in Fig. 14 (a) and Fig. 15 (a). The yield surface remains unchanged because there is no plastic deformation. In the loading analysis step, i.e., the path from stress point 5 to stress point 21, the stress point moves to the yield surface again. The plastic deformation starts to occur after the stress point reaches the yield surface. For element 4, as shown in Fig. 14 (b), the stress point first lies on the 'dry' side of the critical state line, then temporarily travels to the 'wet' side, and eventually returns to the 'dry' side. The change of stress path indicates that the soil around the integral point undergoes a transformation from strain-softening to strain-hardening and back again. Correspondingly, the yield surface shrinks first, then expands, and eventually shrinks again. The stress state of the integral point for element 2260 is

always on the 'wet' side of the critical state line, as shown in Fig. 15 (b). The strain-hardening behaviour is the only thing that is seen. The yield surface is always expanding. It is worth emphasizing that due to the use of the smoothing function, the stress point is always on or inside the yield surface. From the perspective of the unconstrained stress updating strategy, the allowable stress region in Fig. 14 (a) and Fig. 15 (a), including the elastic region and the yield surface, is projected onto a smoothing curve. Whether loading or unloading cases, the stress point is always on the smoothing curve, as shown in Fig. 14 (c) and Fig. 15 (c). The *KKT* conditions are always satisfied due to the fact that the smoothing function is an equivalent approximation of *KKT* conditions.

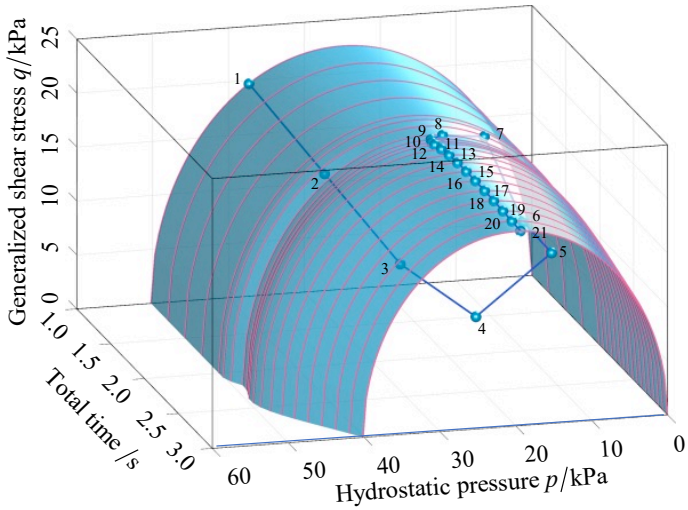

(a)

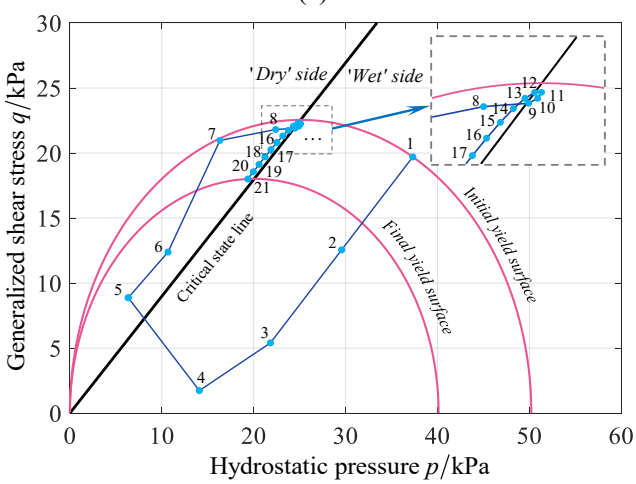

(b)

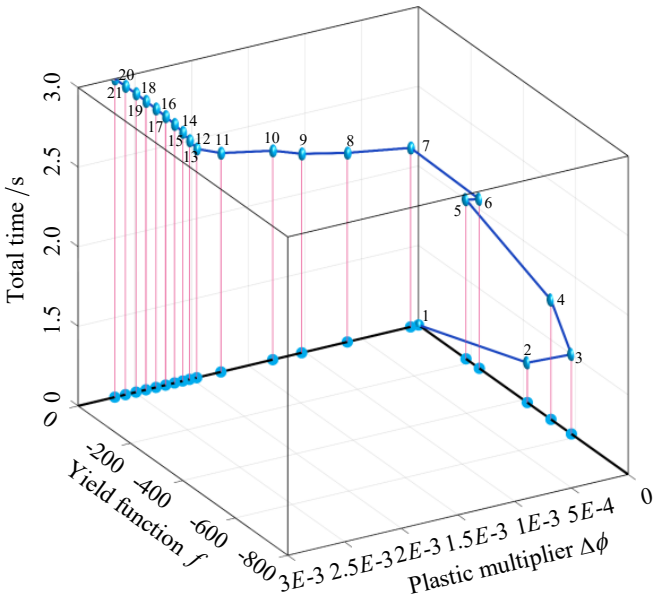

(c)

Fig. 14 Stress path at integral point 8 of element 4: (a) the result in the *p-q-time* coordinate system; (b) the result in the *p-q* coordinate system; (c) the result in the *f*- $\Delta\phi$-*time* coordinate system.

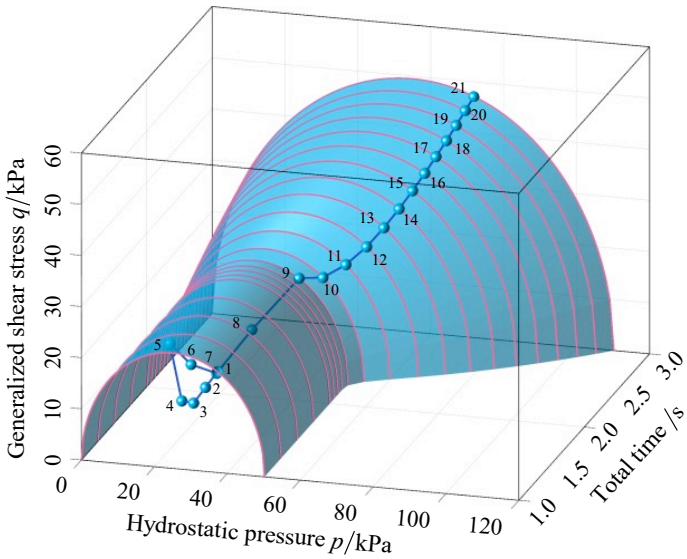

(a)

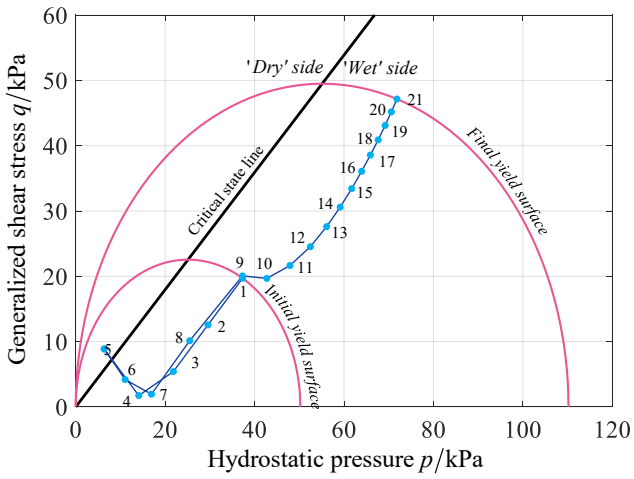

(b)

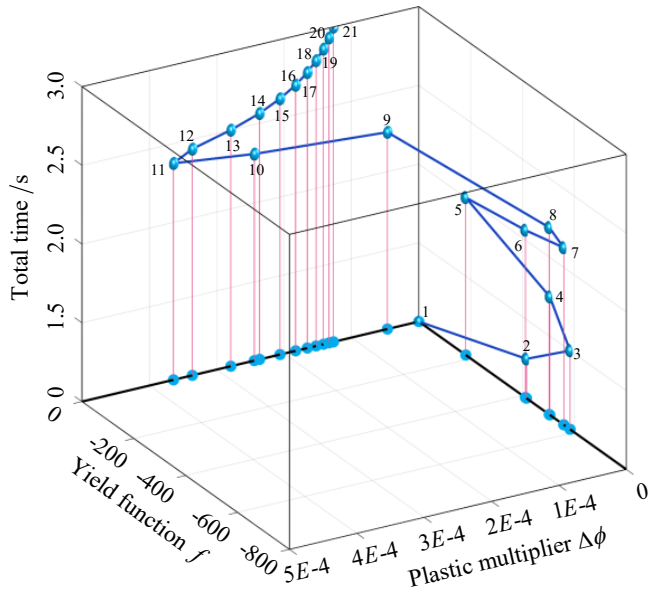

(c)

Fig. 15 Stress path at integral point 8 of element 2260: (a) the result in the *p-q-time* coordinate system; (b) the result in the *p-q* coordinate system; (c) the result in the *f*- $\Delta\phi$-*time* coordinate system.

6.4. Cylindrical sample with cyclically combined tension and shear

The last example is that the cylindrical sample is subjected to cyclically combined tension and shear load. The example is often used to test the numerical implementation of the constitutive model based on the optimization methods (Shterenlikht & Alexander 2012; Lester & Scherzinger 2017; Scherzinger 2017) since it generates a sufficiently hard stress condition to evaluate the algorithm's robustness. Fig. 16 gives the necessary information of the cylindrical specimen and its finite element model where the C3D8 element is employed. The material parameters used for the example are set to $M = 1$, $\lambda = 0.15$, $\kappa = 0.03$, and $\nu = 0.3$. The initial void ratio and the initial stress state are set to $e_0 = 0.5$ and $\sigma_1 = \sigma_2 = \sigma_3 = 200$ kPa. Fig. 17 demonstrates the history curve of displacement load, which is applied on the top surface of the cylinder in 10 loading analysis steps. The initial time increment of each analysis step is 0.1s. The *automatic time incrementation method* of ABAQUS software is used to determine the following size of load increment. The generalized shear stress distribution of the cylinder at the end of the load is shown in Fig. 18 (a). The reaction

force responses of the top surface of the cylinder obtained by the proposed algorithm and ABAQUS/Standard DIM are depicted in Fig. 18 (b). Again, the findings of the two algorithms demonstrate good consistency.

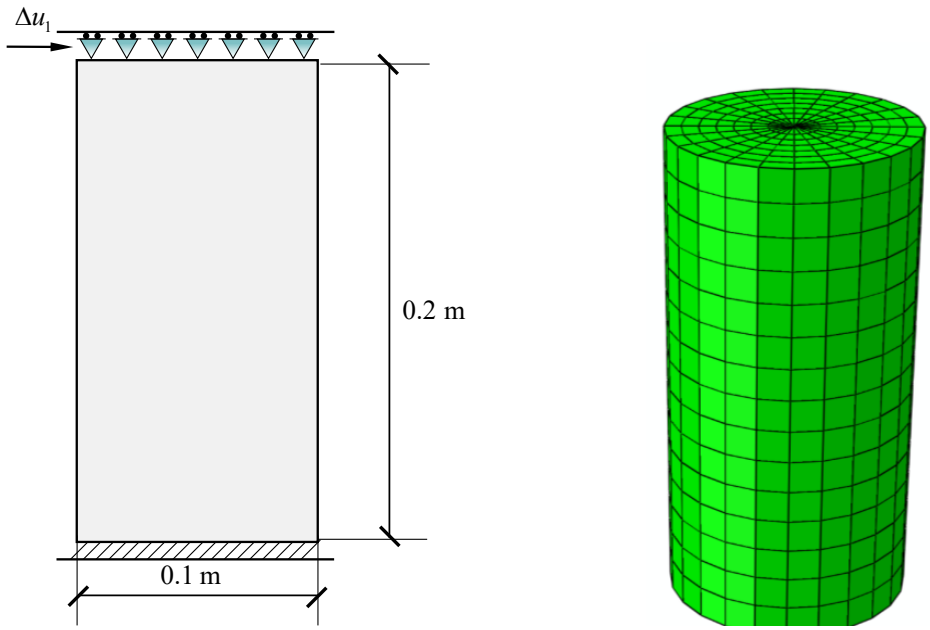

(a) (b)

Fig. 16 Summary of the cylindrical sample with cyclically combined tension and shear: (a) geometry and boundary conditions; (b) mesh

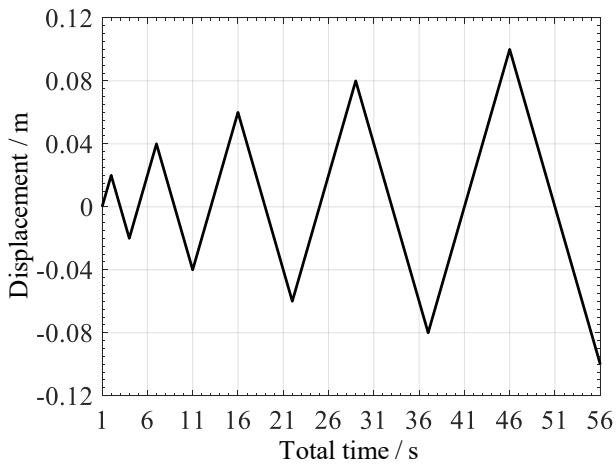

Fig. 17 Time-history curve of displacement load in the 1-direction

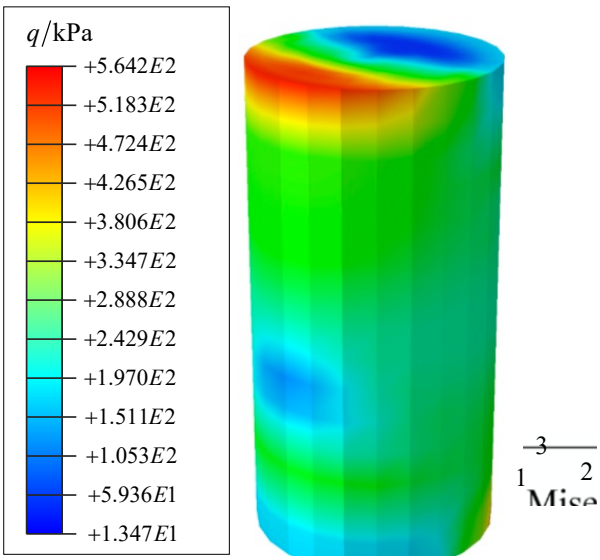

(a)

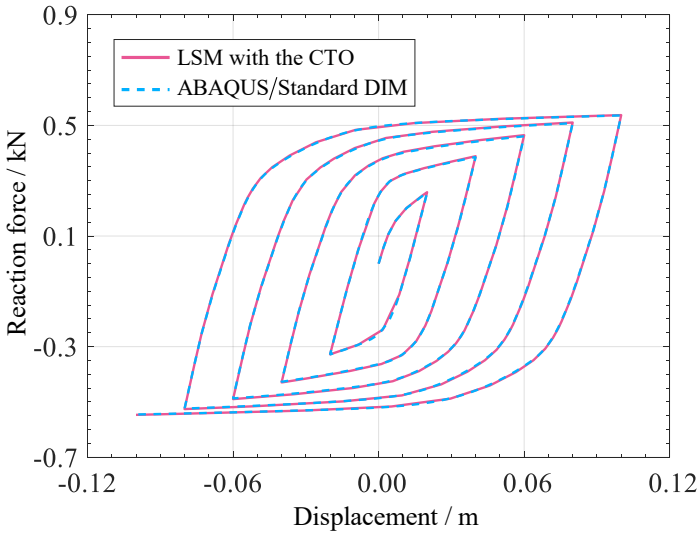

(b)

Fig. 18 Simulation results of the cylindrical sample with cyclically combined tension and shear: (a) generalized shear stress distribution; (b) reaction force response in the 1-direction.

Finally, based on this example with the complex stress states, the computational efficiency and robustness of the proposed algorithm are further evaluated. The CPU time, the number of load increments, and the number of global equilibrium iterations are used as the assessment indices of algorithm performance. Fig. 19 (a) compares the change in the size of load increments for the two algorithms. The result shows that the proposed algorithm allows substantially larger load increments than the ABAQUS/Standard DIM. Correspondingly, the proposed algorithm only spends 40.9% of

the ABAQUS/Standard DIM CPU time and gets almost the same results. The number of global iterations and load increments can also demonstrate the benefits of the proposed algorithm. In the *automatic time incrementation method*, too many failed attempts will prohibit the size of load increment from increasing, requiring more load increments. And the iterations wasted on failed attempts also increase the computational cost. As shown in Fig. 19 (b), the proposed algorithm's calculation rarely encounters the failed attempts. The failed load increments and global iterations of the proposed algorithm are only 10.0% and 17.6% of the ABAQUS/Standard DIM, respectively. Therefore, the size of the load increment of the proposed algorithm keeps increasing trend almost all the time. There are fewer load increments and global iterations required, as shown in Fig. 19 (c), For the representative example, the total number of load increments and the global iterations of the proposed algorithm is only 24.1% and 45.8% of those in the ABAQUS/Standard DIM, respectively.

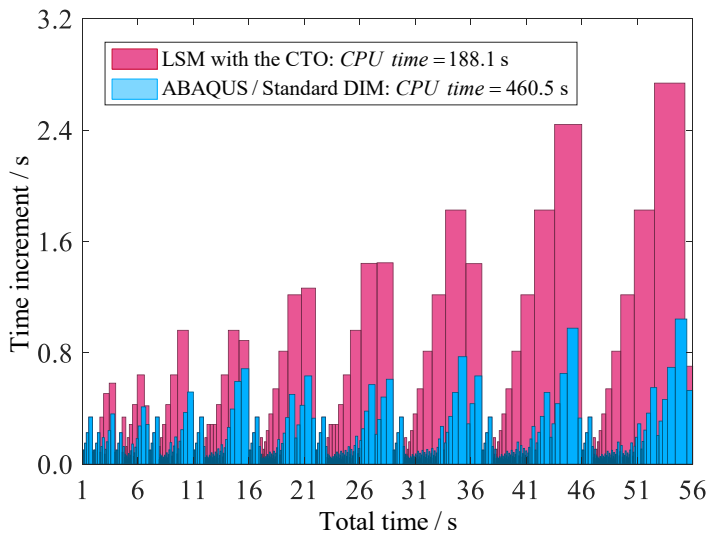

(a)

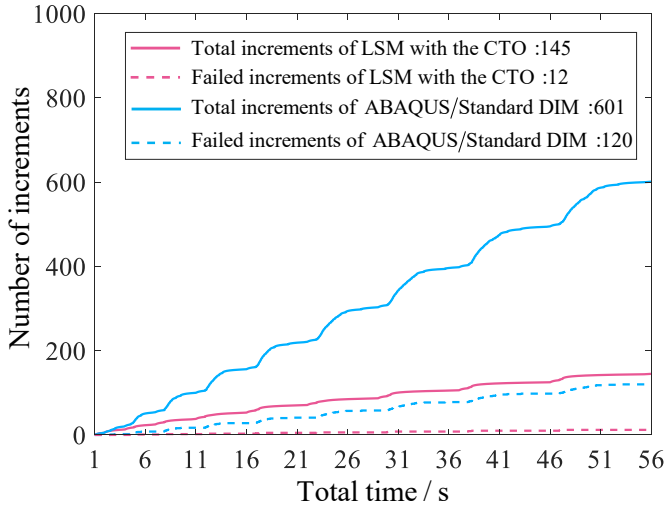

(b)

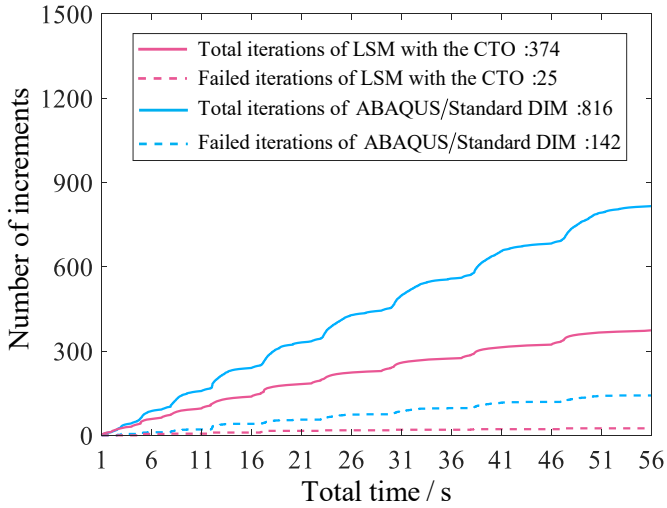

(c)

Fig. 19 Convergence behaviour: (a) the change in the load increment size; (b) the number of load increments; (c) the number of global equilibrium iterations.

Finally, a summary of the comparison between ABAQUS/Standard DIM and the proposed algorithm is given. In the ABAQUS/Standard DIM, the operator splitting technique with the elastic prediction is used to address the loading/unloading inequality constraints. The nonlinear equations are solved by the Newton method. In the proposed algorithm, the non-smoothness caused by the loading/unloading inequality constraints is addressed by the smooth function. Compared with the operator splitting technique, it avoids the loading/unloading estimations in each increment step and unifies the stress integral equations in elastic and elastoplastic cases. On the other hand, the LSM is

used to solve nonlinear equations, which allows a larger convergence radius than the Newton method. Therefore, better robustness and computational efficiency of the proposed algorithm than ABAQUS/Standard DIM are observed in Fig. 19.

7. Conclusion

For the numerical implementation of elastoplastic soil models and even for the elastoplastic model in general, the nonlinearity and nonsmoothness have been the challenges that need to be overcome. This paper presents an efficient and robust stress updating algorithm to address the two problems above. By replacing the *KKT* conditions involving the loading/unloading inequality constraints with the smoothing function, the stress integration equations are transformed into a smooth form, which brings unconstrained stress updating framework. In addition, the stress integration equations and the smoothing CTO corresponding to this stress updating strategy have a unified form regardless of the loading and unloading cases. The benefit is that it provides a concise computational framework for the numerical implementation of the model, and it also avoids the nonsmoothness of the elastoplastic problem.

On the other hand, the nonlinearity of the constitutive model may lead to the solution divergence at the local calculation, particularly for a larger strain increment input. The proposed algorithm improves the solution's convergence by using the LSM, which considerably reduces the possibility of local calculation failure caused by the model nonlinearity and a step size that is too large. The computation cost is reduced since the finite element calculation can be completed in fewer increment steps. In the representative example presented in Section 6.4, the number of load increments and global iteration of the proposed algorithm spent on the failed attempts is only 10.0%

and 17.6% of the ABAQUS/Standard DIM. The CPU time required by the proposed algorithm is only 40.9% of that needed for the ABAQUS/Standard DIM. This superior performance ensures the efficient numerical analysis of geotechnical engineering problems and brings a prospect worth applying the proposed algorithm in other elastoplastic models.

Data availability statement

The UMAT code is open-source and downloadable from https://github.com/zhouxin615/Stress_Updating_Algorithm.

Acknowledgments

Support for this study is provided by the National Natural Science Foundation of China (Grant Nos., 52025084 and 51778026).

Appendix: elements in the Jacobian matrix

To facilitate the derivation of the Jacobian matrix $\left[\nabla \mathbf{f}(\mathbf{x})\right]_{n+1}$ of residual equations in Eq. (18), the derivatives of $\Delta\varepsilon_{\mathrm{v},\,n+1}^{\mathrm{e}}$ with respect to the unknown variables p_{n+1}, q_{n+1}, $p_{\mathrm{c},\,n+1}$, and $\Delta\phi_{n+1}$ are derived first. $\Delta\varepsilon_{\mathrm{v},\,n+1}^{\mathrm{e}}$ can be expressed as follows:

$$\Delta\varepsilon_{\mathrm{v},\,n+1}^{\mathrm{e}} = \Delta\varepsilon_{\mathrm{v},\,n+1} - \Delta\varepsilon_{\mathrm{v},\,n+1}^{\mathrm{p}} = \Delta\varepsilon_{\mathrm{v},\,n+1} - \Delta\phi_{n+1}\left(2p_{n+1} - p_{\mathrm{c},\,n+1}\right) \tag{47}$$

Taking the derivative of Eq. (47), we can obtain:

$$\begin{cases} \dfrac{\partial \Delta\varepsilon_{\mathrm{v},\,n+1}^{\mathrm{e}}}{\partial p_{n+1}} = -2\Delta\phi_{n+1} \\ \dfrac{\partial \Delta\varepsilon_{\mathrm{v},\,n+1}^{\mathrm{e}}}{\partial q_{n+1}} = 0 \\ \dfrac{\partial \Delta\varepsilon_{\mathrm{v},\,n+1}^{\mathrm{e}}}{\partial p_{\mathrm{c},\,n+1}} = \Delta\phi_{n+1} \\ \dfrac{\partial \Delta\varepsilon_{\mathrm{v},\,n+1}^{\mathrm{e}}}{\partial \Delta\phi_{n+1}} = p_{\mathrm{c},\,n+1} - 2p_{n+1} \end{cases} \tag{48}$$

Then, the derivatives of the secant shear modulus $\bar{G}$ with respect to the unknown variables p_{n+1}, q_{n+1}, $p_{\mathrm{c},\,n+1}$, and . $\Delta\phi_{n+1}$. can be easily obtained. The expression of $\bar{G}$ is:

$$\bar{G} = \frac{p_n}{\Delta\varepsilon^{\mathrm{e}}_{\mathrm{v},\,n+1}} \exp\left[\left(\frac{1+e}{\kappa}\Delta\varepsilon^{\mathrm{e}}_{\mathrm{v},\,n+1}\right) - 1\right] r \tag{49}$$

Based on the chain rule, we can obtain:

$$\begin{cases} \dfrac{\partial\bar{G}}{\partial p_{n+1}} = \dfrac{\partial\bar{G}}{\partial\Delta\varepsilon^{\mathrm{e}}_{\mathrm{v},\,n+1}}\dfrac{\partial\Delta\varepsilon^{\mathrm{e}}_{\mathrm{v},\,n+1}}{\partial p_{n+1}} = -2\dfrac{K_{n+1}-\bar{K}}{\Delta\varepsilon_{\mathrm{v},\,n+1}-\Delta\varepsilon^{\mathrm{p}}_{\mathrm{v},\,n+1}} r\Delta\phi_{n+1} \\ \dfrac{\partial\bar{G}}{\partial q_{n+1}} = \dfrac{\partial\bar{G}}{\partial\Delta\varepsilon^{\mathrm{e}}_{\mathrm{v},\,n+1}}\dfrac{\partial\Delta\varepsilon^{\mathrm{e}}_{\mathrm{v},\,n+1}}{\partial q_{n+1}} = 0 \\ \dfrac{\partial\bar{G}}{\partial p_{\mathrm{c},\,n+1}} = \dfrac{\partial\bar{G}}{\partial\Delta\varepsilon^{\mathrm{e}}_{\mathrm{v},\,n+1}}\dfrac{\partial\Delta\varepsilon^{\mathrm{e}}_{\mathrm{v},\,n+1}}{\partial p_{\mathrm{c},\,n+1}} = \dfrac{K_{n+1}-\bar{K}}{\Delta\varepsilon^{\mathrm{e}}_{\mathrm{v},\,n+1}} r\Delta\phi_{n+1} \\ \dfrac{\partial\bar{G}}{\partial\Delta\phi_{n+1}} = \dfrac{\partial\bar{G}}{\partial\Delta\varepsilon^{\mathrm{e}}_{\mathrm{v},\,n+1}}\dfrac{\partial\Delta\varepsilon^{\mathrm{e}}_{\mathrm{v},\,n+1}}{\partial\Delta\phi_{n+1}} = -\dfrac{K^{k}_{n+1}-\bar{K}}{\Delta\varepsilon^{\mathrm{e}}_{\mathrm{v},\,n+1}} r\left(2p_{n+1}-p_{\mathrm{c},\,n+1}\right) \end{cases} \tag{50}$$

In what follows, the elements in the Jacobian matrix of the residual equation are given successively. The derivatives of f_1 are:

$$\begin{cases} f_{1,1} = \dfrac{\partial f_1}{\partial p_{n+1}} = 1 + 2\Delta\phi_{n+1}K_{n+1} \\ f_{1,2} = \dfrac{\partial f_1}{\partial q_{n+1}} = 0 \\ f_{1,3} = \dfrac{\partial f_1}{\partial p_{\mathrm{c},\,n+1}} = -\Delta\phi_{n+1}K_{n+1} \\ f_{1,4} = \dfrac{\partial f_1}{\partial\Delta\phi_{n+1}} = c_{\mathrm{d}}\left(2p_{n+1}-p_{\mathrm{c},\,n+1}\right)K_{n+1} \end{cases} \tag{51}$$

The derivatives of f_2 are:

$$\begin{cases} f_{2,1} = \dfrac{\partial f_2}{\partial p_{n+1}} = -\sqrt{\dfrac{3}{2}}\eta\dfrac{\partial\bar{G}}{\partial p_{n+1}}\left(2\hat{\mathbf{n}}:\Delta\boldsymbol{\gamma}_{n+1} - \dfrac{6\eta\Delta\phi_{n+1}}{M^2}\left\|\mathbf{s}_n + 2\bar{G}\Delta\boldsymbol{\gamma}_{n+1}\right\|\right) \\ f_{2,2} = \dfrac{\partial f_2}{\partial q_{n+1}} = 1 \\ f_{2,3} = \dfrac{\partial f_2}{\partial p_{\mathrm{c},\,n+1}} = -\sqrt{\dfrac{3}{2}}\eta\dfrac{\partial\bar{G}}{\partial p_{\mathrm{c},\,n+1}}\left(2\hat{\mathbf{n}}:\Delta\boldsymbol{\gamma}_{n+1} - \dfrac{6\eta\Delta\phi_{n+1}}{M^2}\left\|\mathbf{s}_n + 2\bar{G}\Delta\boldsymbol{\gamma}_{n+1}\right\|\right) \\ f_{2,4} = \dfrac{\partial f_2}{\partial\Delta\phi_{n+1}} = -\sqrt{\dfrac{3}{2}}\eta\left[2\hat{\mathbf{n}}:\Delta\boldsymbol{\gamma}_{n+1}\dfrac{\partial\bar{G}}{\partial\Delta\phi_{n+1}} - \dfrac{6\eta}{M^2}\left\|\mathbf{s}_n + 2\bar{G}\Delta\boldsymbol{\gamma}_{n+1}\right\|\left(\Delta\phi_{n+1}\dfrac{\partial\bar{G}}{\partial\Delta\phi_{n+1}} + \bar{G}\right)\right] \end{cases} \tag{52}$$

where

$$\eta = \frac{1}{1 + 6\bar{G}\Delta\phi_{n+1} / M^2} \tag{53}$$

The derivatives of f_3 are:

$$\begin{cases} f_{3,1} = \dfrac{\partial f_3}{\partial p_{n+1}} = -2c_{\mathrm{p}}\Delta\phi_{n+1} p_{\mathrm{c},\,n} \exp\left[c_{\mathrm{p}}\Delta\phi_{n+1}\left(2p_{n+1} - p_{\mathrm{c},\,n+1}\right)\right] \\ f_{3,2} = \dfrac{\partial f_3}{\partial q_{n+1}} = 0 \\ f_{3,3} = \dfrac{\partial f_3}{\partial p_{\mathrm{c},\,n+1}} = 1 + c_{\mathrm{p}}\Delta\phi_{n+1} p_{\mathrm{c},\,n} \exp\left[c_{\mathrm{p}}\Delta\phi_{n+1}\left(2p_{n+1} - p_{\mathrm{c},\,n+1}\right)\right] \\ f_{3,4} = \dfrac{\partial f_3}{\partial \Delta\phi_{n+1}} = -c_{\mathrm{p}}\left(2p_{n+1} - p_{\mathrm{c},\,n+1}\right) p_{c,\,n} \exp\left[c_{\mathrm{p}}\Delta\phi_{n+1}\left(2p_{n+1} - p_{\mathrm{c},\,n+1}\right)\right] \end{cases} \tag{54}$$

The derivatives of f_4 are:

$$\begin{cases} f_{4,1} = \dfrac{\partial f_4}{\partial p_{n+1}} = \chi_0\left(2p_{n+1} - p_{c,\,n+1}\right) \\ f_{4,2} = \dfrac{\partial f_4}{\partial q_{n+1}} = \chi_0 \dfrac{2q_{n+1}}{M^2} \\ f_{4,3} = \dfrac{\partial f_4}{\partial p_{\mathrm{c},\,n+1}} = -\chi_0 p_{n+1} \\ f_{4,4} = \dfrac{\partial f_4}{\partial \Delta\phi_{n+1}} = \chi_1 \end{cases} \tag{55}$$

List of figure captions

Fig. 1 Operator splitting stress updating strategy.

Fig. 2 Smoothing curves with the different values of β.

Fig. 3 Unconstrained stress updating strategy.

Fig. 4 Flow chart of unconstrained stress updating algorithm using the LSM.

Fig. 5 Summary of cylindrical cavity expansion: (a) original boundary problem; (b) simplified model and mesh.

Fig. 6 Comparison between the proposed algorithm and analytical solution under undrained conditions: (a) OCR = 1; (b) OCR = 3; (c) OCR = 10.

Fig. 7 Comparison between the proposed algorithm and analytical solution under drained conditions: (a) OCR = 1; (b) OCR = 3; (c) OCR = 10.

Fig. 8 Summary of tunnel excavation: (a) geometry and boundary conditions; (b) mesh.

Fig. 9 Simulation results of tunnel excavation: (a) displacement field in the 3-direction; (b) ground surface settlement curves.

Fig. 10 Summary of bearing capacity test of foundation: (a) geometry and boundary conditions; (b) mesh.

Fig. 11 Simulation results of bearing capacity test of foundation: (a) generalized shear stress distribution; (b) footing load versus footing displacement.

Fig. 12 Convergence behaviour at the critical node: (a) LSM with the CTO and the ABAQUS/Standard DIM; (b) LSM with the CTO and the continuum tangent operator.

Fig. 13 Number of iterations at each load increment: (a) LSM with the continuum tangent operator; (b) LSM with the CTO; (c) ABAQUS/Standard DIM.

Fig. 14 Stress path at integral point 8 of element 4: (a) the result in the *p-q-time* coordinate system; (b) the result in the *p-q* coordinate system; (c) the result in the f- $\Delta\phi$-*time* coordinate system.

Fig. 15 Stress path at integral point 8 of element 2260: (a) the result in the *p-q-time* coordinate system; (b) the result in the *p-q* coordinate system; (c) the result in the f- $\Delta\phi$-*time* coordinate system.

Fig. 16 Summary of the cylindrical sample with cyclically combined tension and shear: (a) geometry and boundary conditions; (b) mesh.

Fig. 17 Time-history curve of displacement load in the 1-direction.

Fig. 18 Simulation results of the cylindrical sample with cyclically combined tension and shear: (a) generalized shear stress distribution; (b) reaction force response in the 1-direction.

Fig. 19 Convergence behaviour: (a) the change in the load increment size; (b) the number of load increments; (c) the number of global equilibrium iterations.

List of table caption

Table 2 Summary of soil properties.

References:

Akpama, H. K., Bettaieb, M. B., Abed Meraim, F., 2016. Numerical integration of rate-independent BCC single crystal plasticity models: comparative study of two classes of numerical algorithms. *Int. J. Numer. Methods Eng.* 108, No. 5, 363-422.

Areias, P., Dias-da-Costa, D., Pires, E. B., Barbosa, J. I., 2012. A new semi-implicit formulation for multiple-surface flow rules in multiplicative plasticity. *Comput. Mech.* 49, No. 5, 545-564.

Areias, P., Rabczuk, T., 2010. Smooth finite strain plasticity with non-local pressure support. *Int. J. Numer. Methods Eng.* 81, 106-134.

Areias, P., Rabczuk, T., César De Sá, J., 2015. Semi-implicit finite strain constitutive integration of porous plasticity models. *Finite Elem. Anal. Des.* 10441-55.

Arora, J. S., 2016. *Introduction to optimum design*, 4th edn. London: Elsevier.

Borja, R. I., 1991. Cam-Clay plasticity, Part II: Implicit integration of constitutive equation based on a nonlinear elastic stress predictor. *Comput. Methods Appl. Mech. Eng.* 88, 225-240.

Borja, R. I., Lee, S. R., 1990. Cam-clay plasticity, part 1: implicit integration of elasto-plastic constitutive relations. *Comput. Methods Appl. Mech. Eng.* 78, 49-72.

Brannon, R. M., Leelavanichkul, S., 2010. A multi-stage return algorithm for solving the classical damage component of constitutive models for rocks, ceramics, and other rock-like media. *Int. J. Frac.* 163, 133-149.

Chen, S. L., Abousleiman, Y. N. 2012. Exact undrained elasto-plastic solution for cylindrical cavity expansion in modified Cam Clay soil. *Géotechnique*. 62, No. 5, 447-456.

Chen, S. L., Abousleiman, Y. N. 2013. Exact drained solution for cylindrical cavity expansion in modified Cam Clay soil. *Géotechnique*. 63, No. 6, 510-517.

Choi, H., Yoon, J. W., 2019. Stress integration-based on finite difference method and its application for anisotropic plasticity and distortional hardening under associated and non-associated flow rules. *Comput. Methods Appl. Mech. Eng.* 345, 123-160.

Contrafatto, L., Cuomo, M., 2005. A globally convergent numerical algorithm for damaging elasto-plasticity based on the Multiplier method. *Int. J. Numer. Methods Eng.* 63, No. 8, 1089-1125.

Dafalias, Y. F., 1980. A bounding surface soil plasticity model. *Proceedings of the ASME Pressure Vessels and Piping Conference*. *Vancoucer* 6, 615-623.

Dutko, M., Perić, D., Owen, D., 1993. Universal anisotropic yield criterion based on superquadric functional representation: part 1. Algorithmic issues and accuracy analysis. *Comput. Methods Appl. Mech. Eng.* 109, 73-93.

Fischer, A., 1992. A special Newton-type optimization method. *Optimization*. 24, 269-284.

Gao, Z. W., Diambra, A., 2021. A multiaxial constitutive model for fibre-reinforced sand. *Géotechnique*. 71, No. 6, 548-560.

Gao, Z. W., Zhao, J. D., Li, X. S., Dafalias, Y. F., 2014. A critical state sand plasticity model accounting

for fabric evolution. *Int. J. Numer. Analyt. Methods Geomech.* 38, No. 4, 370-390.

Gawecka, K. A., Cui, W. J., Taborda, D. M. G., Potts, D. M., Zdravković, L., Loukas, A., 2021. Predictive modelling of thermo-active tunnels in London Clay. *Géotechnique*. 71, No. 8, 735-748.

Geng, D. J., Dai, N., Guo, P. J., Zhou, S. H., Di, H. G., 2021. Implicit numerical integration of highly nonlinear plasticity models. *Comput. Geotech.* 132, 103961.

Hashiguchi, K., 1989. Subloading surface model in unconventional plasticity. *Int. J. Solids Struct.* 25, No. 8, 917-945.

Hernández, J. A., Oliver, J., Cante, J. C., Weyler, R., 2011. A robust approach to model densification and crack formation in powder compaction processes. *Int. J. Numer. Methods Eng.* 87, No. 8, 735-767.

Homel, M. A., Brannon, R. M., 2015. Relaxing the multi-stage nested return algorithm for curved yield surfaces and nonlinear hardening laws. *Int. J. Frac.* 194, No. 1, 51-57.

Homel, M. A., Guilkey, J. E., Brannon, R. M., 2015. Numerical solution for plasticity models using consistency bisection and a transformed-space closest-point return: a nongradient solution method. *Comput. Mech.* 56, No. 4, 565-584.

Kanzow, C., 1996. Some noninterior continuation methods for linear complementarity problems. *Siam J. Matrix Anal. A.* 17, No. 4, 851-868.

Krabbenhoft, K., Lyamin, A. V., 2012. Computational Cam clay plasticity using second-order cone programming. *Comput. Methods Appl. Mech. Eng.* 209-212, 239-249.

Krabbenhoft, K., Lyamin, A. V., Sloan, S. W., Wriggers, P., 2007. An interior-point algorithm for elastoplasticity. *Int. J. Numer. Methods Eng.* 69, No. 3, 592-626.

Lester, B. T., Scherzinger, W. M., 2017. Trust region based return mapping algorithm for implicit integration of elastic-plastic constitutive models. *Int. J. Numer. Methods Eng.* 12, No. 3, 257-282.

Liang, J., Lu, D., Zhou, X., Du, X., Wu, W., 2019. Non-orthogonal elastoplastic constitutive model with the critical state for clay. *Comput. Geotech.* 116, 103200.

Liu, K., Chen, S. L., Voyiadjis, G. Z. 2019. Integration of anisotropic modified Cam Clay model in finite element analysis: Formulation, validation, and application. *Comput. Geotech*. 116, 103198.

Moran, B., Ortiz, M., Shih, C. F., 1990. Formulation of implicit finite element methods for multiplicative finite deformation plasticity. *Int. J. Numer. Methods Eng.* 29, No. 3, 483-514.

Nocedal, J., Wright, S., 2006. *Numerical optimization*. New York: Springer Science & Business Media.

Ortiz, M., Simo, J. C., 1986. An analysis of a new class of integration algorithms for elastoplastic constitutive relations. *Int. J. Numer. Methods Eng.* 23, No. 3, 353-366.

Pérez-Foguet, A., Armero, F., 2002. On the formulation of closest ‐ point projection algorithms in elastoplasticity—part II: Globally convergent schemes. *Int. J. Numer. Methods Eng.* 53, No. 2, 331-374.

Pérez-Foguet, A., Rodríguez-Ferran, A., Huerta, A., 2001. Consistent tangent matrices for substepping schemes. *Comput. Methods Appl. Mech. Eng.* 190, 4627-4647.

Potts, D. M., Cui, W. J., Zdravković, L., 2021. A coupled THM finite element formulation for unsaturated soils and a strategy for its nonlinear solution. *Comput. Geotech.* 136, 104221.

Roscoe, K. H., Burland, J. B., 1968. *On the generalized stress-strain behaviour of wet clay: Engineering Plasticity*. Cambridge: Cambridge University Press.

Roscoe, K. H., Schofield, A. N., 1963. Mechanical behaviour of an idealized 'wet' clay. *Proceeding of*

2nd European Conference on Soil Mechanics & Foundation Engineering. Wiesbaden. 1, 47-54.

Scalet, G., Auricchio, F., 2018. Computational methods for elastoplasticity: an overview of conventional and less-conventional approaches. *Arch. Comput. Method. E.* 25, No. 3, 545-589.

Scherzinger, W. M., 2017. A return mapping algorithm for isotropic and anisotropic plasticity models using a line search method. *Comput. Methods Appl. Mech. Eng.* 317, 526-553.

Schmidt-Baldassari, M., 2003. Numerical concepts for rate-independent single crystal plasticity. *Comput. Methods Appl. Mech. Eng.* 192, 1261-1280.

Schofield, A. N., Wroth, C. P., 1968. *Critical state soil mechanics*. London: McGraw-hill.

Seifert, T., Schmidt, I., 2008. Line-search methods in general return mapping algorithms with application to porous plasticity. *Int. J. Numer. Methods Eng.* 73, No. 10, 1468-1495.

Sheng, D. C., Sloan, S. W., Yu, H. S., 2000. Aspects of finite element implementation of critical state models. *Comput. Mech.* 26, No. 2, 185-196.

Shterenlikht, A., Alexander, N. A., 2012. Levenberg-Marquardt vs Powell's dogleg method for Gurson-Tvergaard-Needleman plasticity model. *Comput. Methods Appl. Mech. Eng.* 237-240, 1-9.

Simo, J. C., Hughes, T. J., 2006. *Computational inelasticity*. New York: Springer Science & Business Media.

Simo, J. C., Ortiz, M., 1985. A unified approach to finite deformation elastoplastic analysis based on the use of hyperelastic constitutive equations. *Comput. Methods Appl. Mech. Eng.* 49, 221-245.

Sloan, S. W., Abbo, A. J., Sheng, D. C., 2001. Refined explicit integration of elastoplastic models with automatic error control. *Eng. Computation.* 18, No. 1/2, 121-194.

Starman, B., Halilovič, M., Vrh, M., Štok, B., 2014. Consistent tangent operator for cutting-plane

algorithm of elasto-plasticity. *Comput. Methods Appl. Mech. Eng.* 272, 214-232.

Sun, D. A., Matsuoka, H., Yao, Y. P., Ichihara, W., 2020. Three-dimensional elasto-plastic model for unsaturated soils. In Unsaturated Soils for Asia): CRC Press, pp. 153-158.

Wang, W., Datcheva, M., Schanz, T., Kolditz, O., 2006. A sub-stepping approach for elasto-plasticity with rotational hardening. *Comput. Mech.* 37, No. 3, 266-278.

Wu, J. Y., Li, J., Faria, R., 2006. An energy release rate-based plastic-damage model for concrete. *Int. J. Solids Struct.* 43, No. 3-4, 583-612.

Xiao, Y., Desai, C. S., 2019. Constitutive modeling for overconsolidated clays based on disturbed state concept. I: Theory. *Int J. Geomech., ASCE* 19, No. 9, 4019101.

Yao, Y. P., Niu, L., Cui, W. J., 2014. Unified hardening (UH) model for overconsolidated unsaturated soils. *Can. Geotech. J.* 51, No. 7, 810-821.

Yoon, S. Y., Lee, S. Y., Barlat, F., 2020. Numerical integration algorithm of updated homogeneous anisotropic hardening model through finite element framework. *Comput. Methods Appl. Mech. Eng.* 372, 113449.

Zhang, W. G., Li, Y. Q., Goh, A., Zhang, R. H., 2020. Numerical study of the performance of jet grout piles for braced excavations in soft clay. *Comput. Geotech*. 124, 103631.

Zhao, J. D., Sheng, D. C., Rouainia, M., Sloan, S. W., 2005. Explicit stress integration of complex soil models. *Int. J. Numer. Analyt. Methods Geomech.* 29, No. 12, 1209-1229.

Zheng, H., Zhang, T., Wang, Q. S., 2020. The mixed complementarity problem arising from non-associative plasticity with non-smooth yield surfaces. *Comput. Methods Appl. Mech. Eng.* 361, 112756.